

# The Lawnmower: an autonomous, protein-based artificial molecular motor

**Authors:** Chapin S. Korosec<sup>1†‡\*</sup>, Ivan Unksov<sup>2†</sup>, Pradheebha Surendiran<sup>2</sup>, Roman Lyttleton<sup>2</sup>, Paul M.G. Curmi<sup>3</sup>, Christopher N. Angstmann<sup>4</sup>, Ralf Eichhorn<sup>5</sup>, Heiner Linke<sup>2\*</sup>, Nancy R. Forde<sup>1\*</sup>

## Affiliations:

<sup>1</sup>Department of Physics, Simon Fraser University, Burnaby, BC, V5A 1S6, Canada.

<sup>2</sup>NanoLund and Solid State Physics, Lund University, Box 118, SE – 22100 Lund, Sweden.

<sup>3</sup>School of Physics, University of New South Wales, Sydney, NSW, 2052, Australia.

<sup>4</sup>School of Mathematics and Statistics, University of New South Wales, Sydney, NSW 2052, Australia.

<sup>5</sup>Nordita, Royal Institute of Technology and Stockholm University, 106 91 Stockholm, Sweden.

\*Corresponding authors. Emails: [chapinkorosec@gmail.com](mailto:chapinkorosec@gmail.com), [heiner.linke@lth.lu.se](mailto:heiner.linke@lth.lu.se), [nforde@sfu.ca](mailto:nforde@sfu.ca)

†These authors contributed equally to this work

‡Current address: Department of Mathematics and Statistics, York University, Toronto, ON, M3J 1P3, Canada

**Abstract:** Inspired by biology, great progress has been made in creating artificial molecular motors. However, the dream of harnessing proteins – the building blocks selected by Nature – to design autonomous motors has so far remained elusive. Here we report the synthesis and characterization of the Lawnmower, an autonomous, protein-based artificial molecular motor comprised of a spherical hub decorated with proteases. Its “burnt-bridge” motion is directed by cleavage of a peptide lawn, promoting motion towards unvisited substrate. We find that Lawnmowers exhibit directional motion with average speeds of up to 80 nm/s, comparable to biological motors. By selectively patterning the peptide lawn on microfabricated tracks, we furthermore show that the Lawnmower is capable of track-guided motion. Our work opens an avenue towards nanotechnology applications of artificial protein motors.

## Main text:

Molecular motors are essential for powering directional motion at the cellular level, including transport and sorting of cargo, cell locomotion and division, and remodelling of the extracellular matrix (1, 2). Biological molecular motors are made of proteins whose directed motion is autonomously coupled to the consumption of chemical free energy. Inspired by such biological machines, significant strides have been made, using small synthetic molecules or DNA as building blocks, to design and implement synthetic devices capable of directed motion on the nanoscale (3-12) and the microscale (12-15). While impressive, these designs have not yet achieved motion along lengthy one-dimensional tracks, akin to cytoskeletal and extracellular filaments and a prerequisite for many potential nanotechnological applications.

Novel motor proteins have been crafted by swapping or re-engineering domains of protein motors (16-22); however, these have been based on naturally occurring motors. Distinct ideas have been proposed for using nonmotor proteins as building blocks to engineer novel motors (12, 20, 23-26), but to our knowledge, motility of a synthetic motor constructed of proteins – the material system that enables the complexity of life – is an important ongoing challenge. Creating a synthetic motor and its track entirely of protein components, which themselves lack motor properties, would demonstrate the abilities of proteins to be used as components of a bioengineering toolbox, and would represent a significant step forward in the field of synthetic biology.

In this work, we demonstrate biased motion of a protein-based synthetic motor dubbed the Lawnmower. The Lawnmower is designed to operate as a burnt-bridges ratchet, whereby it exploits chemical free energy and polyvalency to achieve directed motion on an underlying substrate. We find that the Lawnmower exhibits biased motion on a two-dimensional peptide lawn, and further implement the Lawnmower on one-dimensional peptide lawns microfabricated to produce track-guided motion of this protein-based synthetic design.

Of the many possible approaches for achieving directed motion at the nanoscale, the Lawnmower design employs the burnt-bridge Brownian ratchet (BBR) mechanism (27). Removal of surface-bound substrate sites by a BBR induces a local free energy gradient, which biases the BBR's thermally driven motion towards energy-rich intact substrate sites. Many different biological systems undergo directed motion as BBRs. These include the *Influenza* virus (28-30), bacterial plasmid partitioning (31) and bacterial engulfment (32), and the ligand-depleting migration mechanism of metazoan cells (33). The BBR mechanism appears to be the mechanism of choice for regulated enzymatic degradation of key extracellular scaffolds in animals and plants, including collagen-degrading mammalian matrix-metalloproteases (MMPs) (34, 35), cellulase (36, 37) and chitinase (38, 39). Synthetic BBRs have been created that use DNA to achieve unguided, two-dimensional motion at the nanoscale (6-10, 40) and microscale (13-15). However, to our knowledge, track-guided motion of a BBR motor has not yet been achieved.

As shown schematically in Figure 1A, the Lawnmower (LM) consists of multiple trypsin proteases coupled through a central microspherical hub; these protease “blades” bind to and cleave peptide substrates presented via an F127 polymer brush adhered to a surface (24, 41) (Materials and Methods). Once the LM lands on the surface, diffusion of the central hub allows protease blades to engage nearby peptides in any direction. The initial cleavage and diffusion direction breaks symmetry. The lack of fresh peptides behind the LM creates a free energy gradient and biases diffusion of the LM towards uncleaved peptide “grass” (Figs. 1A, S1). We

expect to see LM dynamics on a two-dimensional peptide lawn exhibiting this biased motility (similar to a self-avoiding walk), whereas on a lawn lacking peptides (referred to as a bare lawn), the LM is expected to exhibit diffusive dynamics (42).

We verified the activity of LMs in solution and compared their peptide cleavage rate to that of trypsin (Fig. S1). We estimate that LMs each accommodate  $(5\pm 1)\cdot 10^5$  active trypsins, or about 0.02 trypsins per  $\text{nm}^2$  of the surface area of the microsphere. Of these,  $\sim 2000$  trypsins can be engaged with the underlying peptide lawn, which presents  $\sim 10^4$  peptides within this LM footprint (Supporting Text). Thus, LMs are active and highly polyvalent, with the potential for thousands of interactions with the lawn.

We observed striking differences between trajectories of LMs on a peptide lawn (peptide-F127) and on a peptide-free, bare lawn (F127) (Figs. 1B, S2, S3). Qualitatively, it is immediately apparent that over similar timescales LMs on peptide lawns travel much farther than on bare lawns. Furthermore, directional bursts can be seen on the peptide lawn, which are not observed on the bare lawn. Thus, the observed LM dynamics on peptide lawns can be described as saltatory (14, 43, 44), in which bursts of long-range travel are interspersed with highly localized, quasi-immotile dynamics (Figs. 1C, S2 and Movie S1). This contrasts with the time-invariant dynamics of LMs on bare lawns, in which essentially all LMs ( $<1\%$  immotile) exhibited diffusive motion (Fig. S3). In fact, while the majority of LMs exhibited motile dynamics on peptide lawns (55%; number of LMs  $n = 59$ ), a significant fraction remained immotile throughout the 12.5-hour experiment ( $n = 49$ ). We classified a LM as “motile” if its mean-squared displacement exceeded a threshold value of  $10\ \mu\text{m}^2$  at  $\tau = 4400\ \text{s}$ , and “immotile” otherwise (Fig. S4A). To correct for sample drift, trajectories of immotile LMs were averaged and this average trajectory was subtracted from each motile LM trajectory (Fig. S4B). Our characterization of LM dynamics focuses on these drift-corrected trajectories of the motile class of LMs: while they may contain transient immotile dwells, they all contain active periods of motility, and the entire trajectories were analysed without internal segregation. Later, we discuss possible reasons for immotility, observed only on peptide lawns.

To quantitatively assess the dynamics of the Lawnmowers on the two types of surfaces, we first followed an approach used for other microscale BBRs (14, 15) and determined how the mean-squared displacement (MSD) of LMs evolves with time, where  $\text{MSD} \propto t^\alpha$ . The scaling of MSD with time characterizes the type of diffusion (45): subdiffusion, conventional diffusion, and superdiffusion correspond to  $0 \leq \alpha < 1$ ,  $\alpha = 1$ , and  $1 < \alpha < 2$ , respectively, while for a purely ballistic system proceeding at a constant velocity,  $\alpha = 2$ . From this picture, LMs with BBR dynamics on peptide lawns should exhibit  $\alpha > 1$ , while LMs on bare lawns should display conventional diffusion with  $\alpha \approx 1$ . We use ensemble-averaging and trajectory-averaging to analyze the MSD, with dynamics characterized by  $\alpha_{\text{EA}}$  and  $\alpha_{\text{TA}}$ , respectively (Eqs. 4, 5). We find that LMs exhibit dynamics consistent with their designed function: trajectories of motile LMs on a peptide lawn are characterized by strongly superdiffusive, ensemble-averaged dynamics at early experimental measurement times ( $\alpha_{\text{EA}} = 1.8$  over tens of minutes), in contrast to the diffusive-like dynamics of LMs on bare lawns ( $\alpha_{\text{EA}} \lesssim 1$ ; Fig. 1D). The isotropic distribution of trajectories at early times confirms that this large value of  $\alpha_{\text{EA}}$  is not due to sample drift (Fig. S5).

A distinct, trajectory-averaged approach to MSD analysis ( $\text{MSD}_{\text{TA}}$ , calculated as a function of time lag  $\tau$  using Eq. 5) further reveals the distinct dynamics of LMs on the two surfaces: on peptide, LMs are characterized by a range of  $\text{MSD}_{\text{TA}}$  values, contrasting strongly with the uniformly diffusive dynamics of LMs on bare lawns (Figs. S4, S6). Comparison of the average

anomalous diffusion exponent from the ensemble of  $\text{MSD}_{\text{TA}}$  indicates that motile LMs retain, on average, superdiffusive dynamics across their entire measured trajectories of 12.5 hours with  $\langle\alpha_{\text{TA}}\rangle = 1.1$  for motile LMs on peptide lawns, while LMs on bare lawns are characterized by  $\langle\alpha_{\text{TA}}\rangle = 0.95$  (Fig. S7), consistent with diffusive behavior. We expect that  $\langle\alpha_{\text{TA}}\rangle = 1.1$  underestimates the superdiffusivity of active LMs because this treatment assumes time-invariant dynamics and averages out the bursts of active motion with the dwells of immotility observed in trajectories on peptide lawns (44). Importantly, the difference between  $\text{MSD}_{\text{EA}}$  and  $\text{MSD}_{\text{TA}}$  indicates that the system is nonergodic (45). This is consistent with the history-dependent dynamics of LMs: their trajectories are influenced by what regions of the peptide lawn they have previously visited and cleaved.

The enhanced motility of LMs on peptide lawns is also revealed by the probability distribution of their displacements  $P(\Delta r)$  and corresponding speeds  $v$ , measured within each  $\Delta t = 10$  s recorded time interval. For LMs on bare lawns, displacement distributions are well described by the Rayleigh distribution for diffusion in 2D and provide expected diffusion coefficients for microscale LMs (Fig. S8 and Supplementary Text). (Gravity holds the LMs against the lawn; the observation of 2D diffusive motion is consistent with the previously demonstrated ability of the F127 surface to block nonspecific adhesion of these microspheres (41).) By contrast, LMs on peptide lawns have heavy-tailed displacement distributions that do not agree with a Rayleigh distribution (Fig. 1E, F). The heavy-tailed displacement distribution of LMs on peptide lawns translates into an approximately three-fold higher mean interval speed of the motile ensemble ( $\langle v \rangle = 58 \pm 20$  nm/s), compared to LMs on bare lawns ( $\langle v \rangle = 23 \pm 4$  nm/s) (errors are standard deviations).

Alternatively, for each LM we determined its average interval speed throughout its trajectory,  $\bar{v} = \overline{\Delta r} / \Delta t$ , where the average displacement per  $\Delta t = 10$  sec interval  $\overline{\Delta r}$  is given by Eq. 3. Even though LMs exhibit extended immotile dwells during their trajectories (Fig. 1C) that decrease their average speed  $\bar{v}$ , nonetheless there is a clear distinction between LM speeds when fuelled by peptides versus on a bare lawn (Fig. 1G). LMs on bare lawns exhibit homogeneous dynamics, possessing trajectory-averaged speeds tightly clustered around  $\bar{v} = 23$  nm/s. By contrast, trajectory-averaged speeds of individual motile LMs on peptide lawns are more broadly distributed and are generally much faster, with 50% of motile LMs having trajectory-averaged speeds of  $\bar{v} = 75 \pm 5$  nm/s. The broad distribution in mean speeds is consistent with the heterogeneity in dynamics on peptide lawns revealed by other metrics (Figs. 1C, S2, S4). Although diffusion may be an effective means of exploring local space at short timescales, the coupling of chemical energy to directed motion allows molecular motors to travel much farther at longer timescales than is possible under thermal diffusion. We see this motor-associated greater range of motion for peptide-fueled versus diffusing LMs clearly demonstrated even at our shortest observation times of 10 seconds, where the average distance travelled is  $\langle \overline{\Delta r} \rangle = 580 \pm 200$  nm on peptide lawn versus the diffusive  $\langle \overline{\Delta r} \rangle = 230 \pm 40$  nm on bare lawns.

Performance measures of our protein-based LMs can be compared with DNA-based microscopic BBRs. The microsphere-based Par design of Vecchiarelli *et al.* represents an *in vitro* reconstitution of the natural BBR-type plasmid partitioning system in *E. coli* (14), and had an average speed of 100 nm/s. Somewhat lower average speeds of 30-50 nm/s were achieved by highly polyvalent DNA motors (HPDMs), a synthetic microscale BBR system (15). These speeds are comparable to the average speed of  $\approx 60$  nm/s exhibited by motile LMs on peptide lawns. The appearance of trajectories differs among these systems: Par trajectories were generally quite straight, while HPDMs moved in a less directed fashion. In our LMs, active

bursts on peptide lawns appear directional (Fig. 1B; Movie S1), while the more localized dynamics appear more isotropic. Quantifying this distinction, we found that active runs of LMs on peptide lawns are directionally persistent: a large step is likely to continue in the same direction as the previous step (Fig. 1H). This is consistent with a BBR mechanism. By contrast, short-range dynamics are directionally anticorrelated (Fig. S9). Anticorrelated step directions can be caused by an effective restoring force presented by the polyvalent binding interactions between trypsins and peptides on the lawn. Simulations of spherical BBRs on 2D landscapes have shown that directional persistence is influenced by both the polyvalency and entropic stiffness of these motor-track binding interactions (42), which may account for some of the differences observed among these different realizations of microscale BBRs.

Track-guided motility is a ubiquitous mechanism of biological molecular motors (1). Furthermore, guidance of cytoskeletal filaments along microfabricated tracks by biological molecular motors is being intensely explored for applications ranging from biosensing and diagnostics to energy-efficient computation (46-49). For many such applications, it would be of great interest to develop custom-made protein motors with bespoke properties and capability of moving along a pre-defined track. Thus, following the demonstration of biased motion of LMs on a 2D surface, we investigated whether LM motion could be guided along narrow tracks. We used chemical specificity to deposit peptide lawns or bare lawns onto the bottoms of microfabricated channels (Fig. 2A) (50). Gravity constrained the dense beads within these 0.5  $\mu\text{m}$  deep channels, which provided effective 1D confinement. The channel width of 2.2  $\mu\text{m}$  was chosen narrower than the LM diameter but sufficiently wide to retain polyvalency of LM-track interactions. Simultaneously tracking particles in orthogonal sets of channels (vertical and horizontal in Fig. 2B) allowed us to check for background flow.

We observed the dynamics of LMs to be guided by these quasi-1D tracks, both for LMs on peptide lawn and particles on bare lawn (Fig. 2B and Movies S2-S5). The evolution of the first and second moments of the displacement distribution of LMs on peptide lawns reveals a small background flow of about 0.01  $\mu\text{m}/\text{s}$  (direction indicated by arrow in Fig. 2B) and a diffusion coefficient of 0.06  $\mu\text{m}^2/\text{s}$ .

There is compelling evidence that LMs exhibit enzymatically driven motion in channels, interspersed with diffusive motion and immotile periods (examples are shown in Movies S3, S4). First, similar to the 2D case, LMs on tracks transition between motile and immotile states when on a peptide lawn (Fig. 2C) while particles on bare lawns exhibit time-invariant dynamics (Fig. 2D). Second, these LM displacement distributions  $P(\Delta x)$  exhibit heavy tails. This is seen by the heightened probability of large displacements for LMs on peptide lawns relative to a Gaussian distribution, whereas displacements in bare lawn channels exhibit the expected Gaussian distribution associated with 1D diffusion (Fig. 2E, F). The shape of the displacement distribution can be quantified by its kurtosis (eq. 8), which indicates the tailedness of a distribution: for a Gaussian distribution,  $\kappa = 3.0$ . For LMs on peptide lawn channels, we find a kurtosis  $\kappa = 3.3$ , indicating larger displacements than expected from a normal distribution. In contrast, particles on bare lawn have  $\kappa = 3.0$ , the expected value for one-dimensional diffusive motion.

To validate these observations of heavy-tailed distributions associated with motor activity, we developed a simple model according to which enzymatic LM action initially creates an area of bare lawn inside a channel. Subsequent LM action can take place only at the left or right edge of the bare area and is interrupted by free diffusion (for more details of this model see Materials and Methods and Fig. S10). In this model, the role of the observed small background flow is to bias LM action towards one side, consistent with the overall directionality apparent in Fig 2B. Data

modelled in this way show a kurtosis  $\kappa = 3.2$ , consistent with the heavy tails observed in experiments (Fig. 2E).

In contrast to this simple model, we do not expect that in the experiment a completely bare lawn is created at first contact with a LM. To check for this, we statistically analyzed the magnitude of LM displacements in the experiment conditioned on whether they occur near the edge of previously unvisited regions versus in previously visited regions (Fig. S11). We find larger displacement near the edges, consistent with LM action (the same is not observed in control experiments with bare lawn), but we also observe large displacements in previously visited regions, indicating the presence of remaining lawn.

It is important to note that the periods of subdiffusive, quasi-immotile behavior that we observe both on 2D and in channels are especially likely in highly polyvalent systems such as the LM. Indeed, in some replicates LMs display increased periods of immotility in peptide channels and exhibit a kurtosis  $\kappa \approx 3$  (Fig. S12). Immotile dwells have been observed for the highly polyvalent DNA motors (HPDMs), where immotility was attributed to entrapment within previously visited, product-rich regions (15). We also see evidence of immotility coinciding with previously visited regions: for example, the long dwell from 4-6.5 hours indicated by the red colour in Fig. 1C overlays with the earlier portion of the trajectory indicated in blue (Fig. 1C, inset). Even small-length fluctuations would be sufficient to drive the LM into a previously visited region, which has the potential to lead to stalling due to the extremely high polyvalency of (even very weak) trypsin-product interactions (51, 52). A second mechanism for transient immotility in highly polyvalent systems is the long timescale associated with cleaving the large number of substrates under the footprint of the motor. In nanoscale HPDMs, release from such a state was posited to give rise to large displacements, associated with a heavy tail in the displacement distributions (10). This mechanism was demonstrated in simulations of the reconstituted microscale Par BBRs, which found step size to inversely correlate with the polyvalency of bead-track interactions during trajectories (43). It is likely the same dynamics are at play in LMs on peptide tracks, producing the observed saltatory dynamics and heavy-tailed displacement distributions (Figs. 1E,F; 2E,F).

Thus, although an increase in LM valency may lead to an increase in speed (10, 53), when LM-track interactions are sufficiently high in number, the LM has a higher probability of becoming immotile, as its motion is quenched by the polyvalency of binding interactions (52). Once enough bonds have broken, the LM is able to capture thermal fluctuations and rapidly access nearby peptides, and if cleavage is sufficiently rapid compared to the formation of many new binding interactions, then large-scale motion continues until enough interactions stochastically form to again trap the LM locally in an immotile state (43). Such dynamics appear to be shared among emerging examples of BBRs, and warrant further investigations to optimize performance.

Starting from the initial performance described here, the LM design lends itself to modular design alterations that could be targeted to enhance and rationally explore the BBR mechanism of motility. These include multivalency (24, 52-57); kinetic rates, particularly the appropriate balance of binding, cleavage and diffusion (31, 42, 43, 57-60); and linker length and flexibility (42, 43, 57). Because the LM and track combine to enable the BBR mechanism, changes in the peptide lawn, such as the stiffness of the peptide supports and the surface density and dimensionality of the peptide track, can also be used to improve performance (42, 58, 61). The microscale LM and its concomitant high polyvalency enabled straightforward experimental measurements, but inadvertently may have led to periods of highly localized dynamics. Reducing multivalency to the level where a protein hub (62) could be used to link a small number of

trypsins could create an entirely protein-based BBR closer to the size scale used by Nature. The demonstration that the LM can be guided by tracks opens the door to future experiments using bespoke properties to sort such motors, for instance, by patterning tracks in more complex geometries and with distinct peptide cleavage signals to guide LMs based on their constituent proteases.

Distinct from the related reconstituted Par and synthetic HPDM microscale BBR systems (14, 15), the LM does not rely on the supply of reagents from solution (Par proteins + ATP and RNaseH, respectively) to sustain motion. This offers the advantage of being a modular system that could be implemented in a variety of settings, without the need to maintain a supply of reagents. A drawback is that sustained LM dynamics require activity of its constituent trypsins; inactivated proteins cannot be replaced as easily as the solution-based supply in these other systems. However, in contrast to these solution-reliant BBRs, the free energy of the LM system is supplied within its prepared peptide lawn and thus can be guided by this track. In this aspect, the LM bears more similarity to extracellular biological systems such as collagenases (34), cellulases (36, 37) and chitinases (38), in which the free energy to power directed motion comes from cleavage of the track itself. Like these biological BBRs, the LM operates autonomously to cleave and self-propel along its track.

While BBRs are inherently destructive to their tracks, one can envision pairing such motors to have guiders and followers, for example kinase- and phosphatase-based LMs that work cooperatively to guide each others' paths in complex environments. LMs could also become environmentally responsive, by incorporating pH- and temperature-dependent proteases in their design. Through evolution, Nature arrived at proteins as its responsive, controllable building material; by harnessing proteins for synthetic purposes, we forge their application to a wide range of new problems.

## Methods

**Lawnmower synthesis:** The synthesis of microscale Lawnmowers was adapted from the previous protocol for quantum-dot-based LMs (24). While the operational principle of the Lawnmower is agnostic to the type of protease used in its design, trypsin is used here because of its retention of catalytic activity following a variety of chemical treatments including reduction, thiolation of amines, and subsequent covalent coupling to its thiols (24). Microscale LMs were built around M-270 amine Dynabead hubs (diameter 2.8  $\mu\text{m}$ ; density 1.6  $\text{g}/\text{cm}^3$ ; ThermoFisher 14307D). Reaction conditions were as previously described (24), except that a magnet was used to pellet beads during buffer exchanges and wash steps, and the incubation times were adjusted (50). 20 mM MOPS pH 7.4 buffer is used throughout the synthesis. To synthesize microscale LMs, first, from an M-270 bead stock concentration of  $2 \times 10^9$  beads/mL we pipetted out 10  $\mu\text{l}$  which we washed and resuspended in MOPS buffer according to the manufacturers protocol for bead equilibration. 2 mg of the heterobifunctional crosslinker sulfo-SMCC (sulfosuccinimidyl-4-(N-maleimidomethyl) cyclohexane-1-carboxylate, ThermoFisher A39268) was dissolved in 200-300  $\mu\text{l}$  of buffer. Beads were resuspended in this solution of sulfo-SMCC and incubated for 4 hours with rotary mixing at room temperature. 800  $\mu\text{l}$  of buffer was added to this bead solution, beads were pelleted down and the supernatant removed. The beads were washed three times, each with 1000  $\mu\text{l}$  of buffer to remove all unreacted sulfo-SMCC. In parallel, cysteines on trypsins (Sigma-Aldrich, T1426) were reduced for 60 minutes using TCEP gel (ThermoFisher 77712). 100  $\mu\text{l}$  of 1 mg/ml cysteine-reduced trypsin was then added to the sulfo-SMCC beads,

and these were incubated with rotary mixing for 4 hours at room temperature. After coupling, the total solution volume was brought to 1000  $\mu\text{l}$ , the beads were pelleted, and the supernatant removed; this was repeated 5 additional times to ensure removal of all excess trypsin.

**Lawnmower polyvalency:** To estimate the number of active trypsins per microsphere, we compared the rate of peptide cleavage for LMs and for varied concentration of trypsin in bulk solution. As a fluorogenic peptide was used (see “Lawn preparation” for details), we calculated the cleavage rate as the slope of increasing peptide fluorescence versus time (Figure S1E) in solutions where LMs were incubated with peptides for different times. Fluorescence was measured for solutions in silicone wells (Grace Bio-Labs) glued on a glass coverslip, using a Ti2-E inverted microscope (Nikon) with a Plan Apo  $\lambda$  40x objective and LED illumination at 470 nm. We found that the cleavage rate for LMs at the concentration of  $3 \cdot 10^7 \text{ mL}^{-1}$  (counted in a Reichert Bright-Line Neubauer chamber) corresponds to the cleavage rate of trypsin at  $(2.6 \pm 0.6) \cdot 10^{-8} \text{ M}$  (Figure S1F). Calculating the ratio between these, we obtained on average  $(5 \pm 1) \cdot 10^5$  trypsins per LM, which corresponds to 0.02 trypsins per  $\text{nm}^2$  of the surface area.

**Lawn preparation:** Substrate peptides were presented as a two-dimensional lawn on a glass coverslip, on which they were supported by an F127 (PEG-PPG-PEG) block-copolymer brush. The preparation of the “peptide” (peptide-F127) and “bare” (F127; Sigma P2443) lawns is as previously described and reproduced here (41). The peptide lawn uses an NHS-functionalized F127 (Polymer Source P40768-EOPOEO2NHS) to couple the central lysine of the peptide (fluorescein isothiocyanate (FITC)-Ala-Pro-Ala-Lys-Phe-Phe-Arg-Leu-Lys-4-([4-(dimethylamino)phenyl]azo)benzoic acid (DABCYL), custom order from Biomatik) to the N-hydroxy-succinimidyl ester (NHS) moiety on the F127. The peptides provided as substrates in these LM experiments bridge a fluorophore and quencher, whereby peptide cleavage releases the quencher to solution and the surface-bound products become fluorescent (24, 61). In the current experiments, LM dynamics were tracked using bright-field microscopy, and fluorescence imaging was used only to confirm formation and accessibility of the peptide lawn ((41), Figs. S13, S14).

Glass was prepared for sample chambers as follows. Glass cover slips and slides were placed in 20 M $\Omega$  water and boiled for 10 minutes in a microwave. The glass was removed from water and submersed in acidified methanol (a mixture of equal volumes MeOH and HCl) and sonicated for 45 minutes. Acidified methanol was removed and the glass was rinsed with ddH<sub>2</sub>O 5 times. The glass was then sonicated with ddH<sub>2</sub>O for 5 minutes. Water was removed and then glass was sonicated in concentrated H<sub>2</sub>SO<sub>4</sub> for 45 minutes. Glass was then rinsed with ddH<sub>2</sub>O 5 times and then sonicated in ddH<sub>2</sub>O for 10 minutes. Glass was then dried with airflow and baked at 100°C for 10 minutes to remove remaining water. The slides were immediately silanized following this treatment. To do so, the glass was immersed in fresh Sigmacote (Sigma-Aldrich, SL2-100ML) for 1 minute 30 seconds and then baked for 30 minutes at 100°C.

Glass chambers were constructed as previously described (41), using a glass slide, cover slip and double-sided tape as spacers. A 10% solution of NHS-F127 (or F127) in 1M sodium phosphate buffer pH 6.0 was pipetted into each chamber to completely fill it. Chambers were immediately placed in a hydration chamber and incubated at 4°C for 4 hours. The chambers were flushed with 1000  $\mu\text{l}$  of the same buffer. A solution of 1  $\mu\text{l}$  of peptide stock in DMSO with 59  $\mu\text{l}$  of sodium phosphate buffer, pH 8.0 was created. Then 30  $\mu\text{l}$  of peptide solution was pipetted into each

chamber. Chambers were incubated overnight in a hydration chamber at 4°C. Chambers were flushed with 0.1 M sodium phosphate buffer, pH 7.4 to remove excess peptide. Lawnmowers were then added in sodium phosphate buffer pH 7.4, at an appropriate dilution to provide well spaced trajectories in the field of view.

**Channel preparation:** Microfabricated channels (Fig. 2) were designed to confine the LMs and provide quasi-1D peptide tracks along the channel floors. A difference in composition between the channel walls (hydrophilic) and channel floor (hydrophobic) was exploited to deposit the peptide lawn selectively on the hydrophobic channel floor. We achieved selective hydrophobicity on the channel floors by a combination of fabrication and surface modification. First, a thermally grown 100 nm thick SiO<sub>2</sub> substrate ((100), Siegert Wafer GmbH) was used to form the floors of the channels. Ultrasonic rinsing of the substrates was carried out in acetone and isopropanol at room temperature (5 minutes in each). The substrates were further cleaned using oxygen plasma (Plasma Preen II-862, Plasmatic Systems, Inc., North Brunswick, NJ) to remove any excess organic debris. Subsequently, CSAR 62 (Allresist GmbH, Strausberg, Germany) was spin-coated at 2500 rpm to a 500 nm thickness and was subsequently baked at 180°C for 2 min. Electron beam lithography (Voyager, Raith GmbH, Dortmund, Germany) was used to pattern microchannels on to the resist at an exposure dose of 250 μC/cm<sup>2</sup>. Channels were developed by immersing the substrates in amyl acetate (Sigma-Aldrich, MO, USA) for 90 s, to dissolve the exposed resist, and then rinsed in isopropanol (Sigma-Aldrich, MO, USA) for 30 s to remove the developer from the surface. Dimensions of channels (2.2 μm) were verified by atomic force microscopy (Bruker Icon 300, MA, USA). The developed microchannels were exposed to oxygen plasma (Plasma Preen II-862, Plasmatic Systems, Inc., North Brunswick, NJ) at 5 mbar for 30s, which differentially affects the surface chemistry of the resist walls and the developed track floors (63, 64). Plasma-treated microchannel samples were surface modified using trimethylchlorosilane (TMCS) (Sigma-Aldrich, MO, USA) in vacuum-controlled chamber at 200 mbar, making the channel floors selectively hydrophobic (64) as needed for the F127 attachment (41). Planar SiO<sub>2</sub> substrates without any resist were used as controls to verify the desired hydrophobicity after silanization by contact angle measurement (90±2°). The deposition of F127-peptide was confirmed by detecting the appearance of FITC fluorescence channels after addition of trypsin at 500 μg/mL in 0.1 M sodium phosphate buffer pH = 8 (Figure S13, S14).

**Imaging and tracking Lawnmower motion:** Imaging of LMs was conducted using brightfield microscopy. For 2D experiments, experiments used a Zeiss Axioskop microscope with 10x objective and a FLIR Blackfly camera. Custom software was used to record image frames at 10-second intervals throughout Lawnmower experiments. Experiments on 2D peptide lawns were each run for a total of 12.5 hours, while experiments on 2D bare lawns were run for 6.2 hours. For channel experiments, imaging of LMs in channels relied on the light reflected from the Si substrate. A 40X Nikon objective and Photometrics 95B camera were used in a basic custom-built upright microscope. Experiments in channels were run at 1- or 5-second intervals between frames, for 1.9 or 11.8 hours on peptide lawns, and for 2 hours for unmodified beads on bare lawns. In all 2D experiments, LM density was sufficiently low to maintain non-overlapping trajectories throughout the experiment, while the channel data includes partially overlapping trajectories. LM trajectories were determined from image stacks using the Fiji plugin MTrack2 (65). Trajectories in channels were analyzed for motion parallel and perpendicular to the channel axis. Analysis of channel data considered only portions of trajectories that remained within a given channel (Fig. S15).

## Analytical methods

Displacement distributions of LMs on 2D bare lawns were fit with the Rayleigh distribution for 2D diffusion (66):

$$P(\Delta r, \Delta t) = \frac{\Delta r}{2(D\Delta t + \sigma_t^2)} e^{-\frac{\Delta r^2}{4(D\Delta t + \sigma_t^2)}}. \quad (1)$$

Here,  $\Delta t$  is the time interval over which the displacements  $\Delta r$  were determined,  $D$  is the diffusion coefficient, and  $\sigma_t^2$  is the experimental uncertainty in bead position tracking. To extract  $D$  for each LM, its displacement distribution  $P(\Delta r, \Delta t)$  is computed at increasing  $\Delta t$  intervals, and the linear function  $D\Delta t + \sigma_t^2$  found through fitting to Eq. 1 is used to determine its value of  $D$  (Fig. S8C).

LM interval speeds were calculated from overlapping displacements over each  $\Delta t = 10$  second interval between image frames by

$$v_i = \frac{\Delta r_i}{\Delta t} = \frac{\sqrt{(x_{i+1} - x_i)^2 + (y_{i+1} - y_i)^2}}{\Delta t}, \quad (2)$$

where  $i$  is used to index the time intervals. The average speed of a LM throughout its trajectory was determined with

$$\bar{v} = \overline{\Delta r} / \Delta t = \frac{1}{n\Delta t} \sum_{i=0}^{n-1} \Delta r_i, \quad (3)$$

where  $n\Delta t = T_{msr}$ , the measurement duration of the trajectory (12.5 hours for LMs on 2D peptide lawns and 6.25 hours for LMs on bare 2D lawns).

The mean squared displacement was calculated in two ways denoted by  $\text{MSD}_{\text{EA}}$  and  $\text{MSD}_{\text{TA}}$  (58). The ensemble-averaged  $\text{MSD}_{\text{EA}}$  is computed as a function of absolute time  $t$  for an ensemble of  $N$  trajectories:

$$\text{MSD}_{\text{EA}}(t) \equiv \langle \Delta r^2(0, t) \rangle = \frac{1}{N} \sum_{j=1}^N \Delta r_j^2(0, t). \quad (4)$$

$\Delta r_j(0, t)$  is the displacement of the  $j^{\text{th}}$  Lawnmower at time  $t$ , since the start of its trajectory at time  $t=0$ . The trajectory-averaged  $\text{MSD}_{\text{TA}}$  is computed independently for each trajectory using all displacements occurring for each time lag  $\tau$ :

$$\text{MSD}_{\text{TA},j}(\tau) \equiv \overline{\Delta r_j^2(\tau)} = \frac{\Delta t}{T_{msr,j} - \tau + \Delta t} \sum_{t=0}^{T_{msr,j} - \tau} \Delta r_j^2(t, \tau). \quad (5)$$

$\Delta r_j(t, \tau)$  is the displacement of the  $j^{\text{th}}$  Lawnmower at a time  $\tau$  relative to its position at time  $t$ . The normalization prefactor is the inverse of the number of data points that contribute to the average for each  $\tau$ .  $\Delta t = 10$  s is the time interval over which displacements are recorded in the experiment and  $T_{msr,j}$  is the total measurement duration of the  $j^{\text{th}}$  trajectory; both  $T_{msr,j}$  and  $\tau$  are integer multiples of  $\Delta t$ . To characterize the ensemble behavior of the LMs, the ensemble average of  $\text{MSD}_{\text{TA}}$  is determined:

$$\langle \text{MSD}_{\text{TA}}(\tau) \rangle = \frac{1}{N} \sum_{j=1}^N \text{MSD}_{\text{TA},j}(\tau). \quad (6)$$

Anomalous diffusion exponents  $\alpha$  were determined by the slope of a linear fit of  $\log \text{MSD}_{\text{EA}}$  versus  $\log$  time  $t$  or of  $\log \text{MSD}_{\text{TA}}$  versus  $\log$  time lag  $\tau$ .  $\text{MSD}_{\text{TA}}$  and hence  $\alpha_{\text{TA}}$  were determined to a maximum time lag of  $\tau_{\text{max}} = 0.1 T_{msr}$ , where  $T_{msr}$  is the total measurement duration. We selected  $\tau_{\text{max}}$  of 0.1 to maintain reasonable statistics, as it has been shown that using larger lags (approaching the trajectory length) can result in significant variation of  $\text{MSD}_{\text{TA}}$  for highly heterogeneous systems (67).

Directional persistence of LMs in 2D was assessed via the angular change between consecutive steps in the trajectory. Steps were converted from Cartesian to polar increments. If the trajectory is the set of points,  $(x_i, y_i)$ , then the polar increments are given by

$$(\Delta r_i, \Delta \theta_i) = \left( \sqrt{(x_{i+1} - x_i)^2 + (y_{i+1} - y_i)^2}, \tan^{-1} \frac{y_{i+1} - y_i}{x_{i+1} - x_i} \right) \quad (7)$$

The difference in angular increments,  $\text{Mod}(\Delta \theta_{i+1} - \Delta \theta_i, 2\pi)$ , provides an assessment of directionality: values near zero indicate a persistent step and values near  $\pm\pi$  indicate an anti-persistent step.

Probability distributions of displacements along the channels  $P(\Delta x)$  were compared with Gaussian distributions in two ways. Displacement distributions per one-second frame were extracted from trajectories in peptide lawn channels (Fig. 2C) and in bare lawn channels (Fig. 2D). The kurtosis of each probability distribution was determined:

$$\kappa = \frac{m_4}{\sigma^4} = \frac{\langle (X - \mu)^4 \rangle}{\langle (X - \mu)^2 \rangle^2}. \quad (8)$$

Here,  $m_4$  is the fourth moment,  $\sigma$  the standard deviation, and  $\mu$  the mean of the distribution of displacements  $X$ . A Gaussian distribution has  $\kappa=3$ . Larger values of kurtosis correspond to distributions with heavier tails. We also visualized the difference from a Gaussian distribution by taking the ratio of the measured  $P(\Delta x)$  to a Gaussian distribution  $P_G(\Delta x)$  with the same mean  $\mu$  and standard deviation  $\sigma$ . This ratio highlights the tailedness of measured distributions. For these analyses, immotile periods for LMs in peptide lawn channels were disregarded and trajectories were truncated when LMs became immotile.

**1D LM model:** We modelled the LM by a random walker that is more likely to step towards previously unvisited positions when reaching the front or rear edge of the area it had already explored (Fig. S10). In the region of bare lawn the LM is a usual random walker with probabilities  $q, p$  to jump to the left/right, respectively, with  $p + q = 1$ . For an unbiased random walker,  $p = q = 1/2$ ; an overall net drift can be accounted for by setting  $q = 1/2 - \delta, p = 1/2 + \delta$  ( $-1/2 \leq \delta \leq 1/2$ ). At the edges of the bare region, stepping towards an uncleaved position is favored by the enzymatic action  $a$  ( $0 \leq a \leq 1/2$ ), which adds to the probability of an outward step towards uncleaved lawn and decreases the probability of an inward step towards bare lawn (Fig. S10). If the LM steps to an uncleaved position, this position is cleaved and becomes part of the bare region.

We scaled trajectories from this discrete, dimensionless model to compare with experiment. By choosing 20,000 steps in our model to correspond with one second in experiment, the step size of the random walker and the drift parameter  $\delta$  were scaled to reproduce the experimentally observed diffusivity of the LM and (small) background flow, *i.e.*, the variance  $\sigma^2$  and mean displacement per 1-s frame. This provided a scaling of 2.35 nm per model step size.

For  $a = 0$ , the displacement distribution of the random walker is a Gaussian (kurtosis  $\kappa = 3$ ) by construction, with first and second moments matching the experimental values. To account for the increased statistical weight of large displacements (larger than about  $4\sigma$  of the Gaussian) observed in experiment on peptide channels, enzymatic action in the model was set to  $a = 0.12$ , which resulted in a kurtosis  $\kappa > 3$  consistent with experiment. According to the model, these large displacements occur exclusively at the edges of the bare region, in contrast to what is observed in experiment (see Section ‘‘Statistical Analysis of LM displacements within previously visited regions’’). We attribute this difference to the model assumption of perfect cleavage of the

lawn at first contact with the LM, whereas the experimental LM appears to cleave only part of the lawn, leaving a mixture of cleaved and uncleaved lawn.

Enzymatic action, represented by  $a = 0.12$  in the model, appears to amplify the effect of the drift near the edges, and therefore increases the average displacement per frame. This interplay of drift and enzymatic action biases LM action towards the direction of the background flow. Therefore, we needed to reduce the background drift correction  $\delta$  by almost 40% to correctly reproduce the average displacement per frame observed in experiment ( $\delta = 0.000057$  compared to the value of  $\delta = 0.00009$  for  $a = 0$ ).

### Comparison of experimental and model displacement distributions with Gaussian distributions:

To determine whether LM displacements in channels can be described by normal diffusion, displacement distributions were compared with Gaussian distributions. Displacement distributions per one-second frame were extracted from trajectories in peptide lawn channels (Fig. 2C) and in bare lawn channels (Fig. 2D). Immotile periods for LMs in peptide lawn channels were disregarded: for this analysis, trajectories were truncated when LMs became immotile. The model trajectories were generated by numerical simulations as described above. The resulting displacement distributions were characterized by the following statistical measures: peptide lawn channels: mean displacement  $0.009 \mu\text{m}$ , standard deviation  $\sigma = 0.33 \mu\text{m}$ , kurtosis  $\kappa = 3.3$ ; bare lawn channels: mean displacement  $0.003 \mu\text{m}$ ,  $\sigma = 0.35 \mu\text{m}$ ,  $\kappa = 3.0$ ; 1D LM model: mean displacement  $0.009 \mu\text{m}$ ,  $\sigma = 0.33 \mu\text{m}$ ,  $\kappa = 3.2$ . Note that in all cases a displacement of about  $\pm 1.3 \mu\text{m}$  corresponds to  $4\sigma$ , such that the data for even larger displacements is dominated by statistical fluctuations and therefore has been omitted. A value of  $\kappa > 3$  was found for these LMs in peptide channels at all timelags tested:  $\tau = 1$  s, 5 s and 10 s.

**Statistical analysis of LM displacements within previously visited regions:** The above simple model for a 1D LM suggests that LM displacements should be larger near the edges of a cleaved region, i.e., adjacent to uncleaved lawn where enzymatic action can take place. To find out whether the magnitude of LM displacements in the 1D channel is related to the position at which they occur relative to the border between previously visited and unvisited regions, we performed the following analysis.

We first corrected the whole ensemble of trajectories for the background flow, which was estimated from the mean value of all measured displacements. Given such a drift-corrected experimental trajectory  $x(t_i)$  (with  $x(t_0) = x(0) = 0$ ), where  $t_i$  is the time point at which frame  $i$  has been recorded, we iterated through all time points  $t_i$  ( $i > 0$ ) and kept track of the edges of the region already visited, i.e., we stored the minimal and maximal positions visited before  $t_i$ ,  $x_{\max}(t_i) = \max_{j \leq i} (x(t_j))$  and  $x_{\min}(t_i) = \min_{j \leq i} (x(t_j))$ . We scaled each position  $x(t_i)$  such that the minimal and maximal positions correspond to  $\pm 1$ ,

$$\tilde{x}(t_i) = \frac{2x(t_i) - (x_{\min}(t_i) + x_{\max}(t_i))}{x_{\max}(t_i) - x_{\min}(t_i)}. \quad (9)$$

Then we subdivided the interval from -1 to +1 into 20 histogram bins to count how often a certain displacement  $\Delta x(t_i) = x(t_i) - x(t_{i-1})$  occurred at the scaled position. The displacements were selected by their magnitude in three different ways: (i) we counted *all* displacements, (ii) we counted only displacements larger than  $1\sigma$ , and (iii) we counted only displacements larger than  $2\sigma$ ;  $\sigma$  is the standard deviation of the distribution of all measured

displacements. When restricting to larger displacements, e.g.  $3\sigma$ , statistical fluctuations became dominant, because such large displacements are quite rare.

Even for a simple standard diffusion process (no LM action) the histogram obtained by counting all displacements was non-uniform, and thus hard to interpret. For this reason, we compared the experimental LM histograms to numerically generated histograms for standard diffusion (produced using the experimental diffusion coefficient). We performed this comparison by calculating the ratio between the probability of observing displacements within a specific histogram bin to the probability of observing displacements within the same histogram bin in the diffusion data (and selected by the same magnitude criterion). The results are shown in Fig. S11. Histogram values larger (smaller) than 1 indicate that displacements are observed more (less) frequently at this scaled position in the LM than they are observed in standard diffusive motion. The error bars estimate the statistical uncertainty, and are obtained from the standard deviation among 5 randomly chosen cluster samples of the full data set.

### Data Availability

The datasets generated during and/or analysed during the current study are available from the corresponding author on reasonable request.

### Code Availability

The codes written to perform the analyses presented in this manuscript are available from the corresponding authors upon reasonable request.

### References

1. M. Schliwa, G. Woehlke, Molecular motors. *Nature* **422**, 759 (2003).
2. R. Iino *et al.*, Single-molecule imaging and manipulation of biomolecular machines and systems. *Biochimica et Biophysica Acta (BBA) - General Subjects* **1862**, 241 (2018).
3. M. von Delius, D. A. Leigh, Walking molecules. *Chemical Society Reviews* **40**, 3656 (2011).
4. S. Erbas-Cakmak, D. A. Leigh, C. T. McTernan, A. L. Nussbaumer, Artificial Molecular Machines. *Chemical Reviews* **115**, 10081 (2015).
5. J. Bath, A. J. Turberfield, DNA nanomachines. *Nature Nanotechnology* **2**, 275 (2007).
6. R. Pei *et al.*, Behavior of polycatalytic assemblies in a substrate-displaying matrix. *Journal Of The American Chemical Society* **128**, 12693 (2006).
7. K. Lund *et al.*, Molecular robots guided by prescriptive landscapes. *Nature* **465**, 206 (2010).
8. T.-G. Cha *et al.*, A synthetic DNA motor that transports nanoparticles along carbon nanotubes. *Nat Nano* **9**, 39 (2014).
9. A. Bazrafshan *et al.*, Tunable DNA Origami Motors Translocate Ballistically Over  $\mu\text{m}$  Distances at nm/s Speeds. *Angewandte Chemie International Edition* **59**, 9514 (2020).
10. A. Bazrafshan *et al.*, DNA Gold Nanoparticle Motors Demonstrate Processive Motion with Bursts of Speed Up to 50 nm Per Second. *ACS Nano* **15**, 8427 (2021).
11. A.-K. Pumm *et al.*, A DNA origami rotary ratchet motor. *Nature* **607**, 492 (2022).
12. X. Arqu , T. Pati o, S. S nchez, Enzyme-powered micro- and nano-motors: key parameters for an application-oriented design. *Chemical Science*, (2022).
13. A. Blanchard *et al.*, Highly polyvalent DNA motors generate 100+ piconewtons of force via autochemophoresis. *Nano Letters*, (2019).

14. A. G. Vecchiarelli, K. C. Neuman, K. Mizuuchi, A propagating ATPase gradient drives transport of surface-confined cellular cargo. *Proceedings of the National Academy of Sciences* **111**, 4880 (2014).
15. K. Yehl *et al.*, High-speed DNA-based rolling motors powered by RNase H. *Nat Nano* **11**, 184 (2015).
16. M. Nakamura *et al.*, Remote control of myosin and kinesin motors using light-activated gearshifting. *Nature Nanotechnology* **9**, 693 (2014).
17. N. V. DelRosso, N. D. Derr, Exploiting molecular motors as nanomachines: the mechanisms of de novo and re-engineered cytoskeletal motors. *Curr. Opin. Biotechnol.* **46**, 20 (2017).
18. K. y. Furuta, A. Furuta, Re-engineering of protein motors to understand mechanisms biasing random motion and generating collective dynamics. *Curr. Opin. Biotechnol.* **51**, 39 (2018).
19. R. Iino, K. Kinbara, Z. Bryant, Introduction: Molecular Motors. *Chemical Reviews* **120**, 1 (2020).
20. H. Linke, B. Höcker, K. y. Furuta, N. R. Forde, P. M. G. Curmi, Synthetic biology approaches to dissecting linear motor protein function: towards the design and synthesis of artificial autonomous protein walkers. *Biophysical Reviews* **12**, 1041 (2020).
21. P. V. Ruijgrok *et al.*, Optical control of fast and processive engineered myosins in vitro and in living cells. *Nature Chemical Biology* **17**, 540 (2021).
22. R. Ibusuki *et al.*, Programmable molecular transport achieved by engineering protein motors to move on DNA nanotubes. *Science* **375**, 1159 (2022).
23. E. H. C. Bromley *et al.*, The Tumbleweed: towards a synthetic protein motor. *HFSP Journal* **3**, 204 (2009).
24. S. Kovacic *et al.*, Design and Construction of the Lawnmower, An Artificial Burnt-Bridges Motor. *IEEE Transactions on NanoBioscience* **14**, 305 (2015). doi: 10.1109/TNB.2015.2393872
25. L. S. R. Small *et al.*, The bar-hinge motor: a synthetic protein design exploiting conformational switching to achieve directional motility. *New Journal of Physics* **21**, 013002 (2019).
26. A. Courbet *et al.*, Computational design of mechanically coupled axle-rotor protein assemblies. *Science* **376**, 383 (2022).
27. T. Antal, P. L. Krapivsky, "Burnt-bridge" mechanism of molecular motor motion. *Physical Review E* **72**, 046104 (2005).
28. T. Sakai, S. I. Nishimura, T. Naito, M. Saito, Influenza A virus hemagglutinin and neuraminidase act as novel motile machinery. *Scientific Reports* **7**, 45043 (2017).
29. M. D. Vahey, D. A. Fletcher, Influenza A virus surface proteins are organized to help penetrate host mucus. *eLife* **8**, e43764 (2019).
30. P. H. Hamming, N. J. Overeem, J. Huskens, Influenza as a molecular walker. *Chemical Science* **11**, 27 (2020).
31. L. Hu, A. G. Vecchiarelli, K. Mizuuchi, K. C. Neuman, J. Liu, Brownian Ratchet Mechanism for Faithful Segregation of Low-Copy-Number Plasmids. *Biophysical Journal* **112**, 1489 (2017).
32. D. H. Broder, K. Pogliano, Forespore Engulfment Mediated by a Ratchet-Like Mechanism. *Cell* **126**, 917 (2006).

33. A. Sarkar, D. N. LeVine, N. Kuzmina, Y. Zhao, X. Wang, Cell Migration Driven by Self-Generated Integrin Ligand Gradient on Ligand-Labile Surfaces. *Current Biology* **30**, 4022 (2020).
34. S. Saffarian, I. E. Collier, B. L. Marmer, E. L. Elson, G. Goldberg, Interstitial Collagenase Is a Brownian Ratchet Driven by Proteolysis of Collagen. *Science* **306**, 108 (2004).
35. S. K. Sarkar, B. Marmer, G. Goldberg, K. C. Neuman, Single-Molecule Tracking of Collagenase on Native Type I Collagen Fibrils Reveals Degradation Mechanism. *Current Biology* **22**, 1047 (2012).
36. K. Igarashi *et al.*, High Speed Atomic Force Microscopy Visualizes Processive Movement of *Trichoderma reesei* Cellobiohydrolase I on Crystalline Cellulose. *Journal of Biological Chemistry* **284**, 36186 (2009).
37. S. K. Brady, S. Sreelatha, Y. Feng, S. P. S. Chundawat, M. J. Lang, Cellobiohydrolase I from *Trichoderma reesei* degrades cellulose in single cellobiose steps. *Nature Communications* **6**, 10149 (2015).
38. A. Nakamura, K.-i. Okazaki, T. Furuta, M. Sakurai, R. Iino, Processive chitinase is Brownian monorail operated by fast catalysis after peeling rail from crystalline chitin. *Nature Communications* **9**, 3814 (2018).
39. A. Nakamura *et al.*, Crystalline chitin hydrolase is a burnt-bridge Brownian motor. *Biophysics and Physicobiology* **17**, 51 (2020).
40. J. Valero, M. Famulok, Regeneration of Burnt Bridges on a DNA Catenane Walker. *Angewandte Chemie International Edition* **59**, 16366 (2020).
41. M. W. H. Kirkness, C. S. Korosec, N. R. Forde, Modified Pluronic F127 Surface for Bioconjugation and Blocking Nonspecific Adsorption of Microspheres and Biomacromolecules. *Langmuir* **34**, 13550 (2018).
42. C. S. Korosec *et al.*, Substrate stiffness tunes the dynamics of polyvalent rolling motors. *Soft Matter* **17**, 1468 (2021).
43. L. Hu, A. G. Vecchiarelli, K. Mizuuchi, K. C. Neuman, J. Liu, Directed and persistent movement arises from mechanochemistry of the ParA/ParB system. *Proceedings of the National Academy of Sciences* **112**, E7055 (2015).
44. O. Osunbayo *et al.*, Complex nearly immotile behaviour of enzymatically driven cargos. *Soft Matter* **15**, 1847 (2019).
45. R. Metzler, J.-H. Jeon, A. G. Cherstvy, E. Barkai, Anomalous diffusion models and their properties: non-stationarity, non-ergodicity, and ageing at the centenary of single particle tracking. *Physical Chemistry Chemical Physics* **16**, 24128 (2014).
46. H. Hess, G. Saper, Engineering with Biomolecular Motors. *Accounts of Chemical Research* **51**, 3015 (2018).
47. M. Lard *et al.*, Ultrafast molecular motor driven nanoseparation and biosensing. *Biosensors and Bioelectronics* **48**, 145 (2013).
48. D. V. Nicolau *et al.*, Parallel computation with molecular-motor-propelled agents in nanofabricated networks. *Proceedings of the National Academy of Sciences* **113**, 2591 (2016).
49. F. C. M. J. M. van Delft *et al.*, Roadmap for network-based biocomputation. *Nano Futures* **6**, 032002 (2022).
50. I. N. Unksov *et al.*, Through the Eyes of Creators: Observing Artificial Molecular Motors. *ACS Nanoscience Au* **2**, 140 (2022).

51. J. Otlewski, F. Jelen, M. Zakrzewska, A. Oleksy, The many faces of protease–protein inhibitor interaction. *The EMBO Journal* **24**, 1303 (2005).
52. A. Kowalewski, N. R. Forde, C. S. Korosec, Multivalent Diffusive Transport. *The Journal of Physical Chemistry B* **125**, 6857 (2021).
53. L. Samii *et al.*, Time-dependent motor properties of multipedal molecular spiders. *Physical Review E* **84**, 031111 (2011).
54. M. J. Olah, D. Stefanovic, Superdiffusive transport by multivalent molecular walkers moving under load. *Physical Review E* **87**, 062713 (2013).
55. C. S. Korosec, M. J. Zuckermann, N. R. Forde, Dimensionality-dependent crossover in motility of polyvalent burnt-bridges ratchets. *Physical Review E* **98**, 032114 (2018).
56. A. T. Blanchard, Burnt bridge ratchet motor force scales linearly with polyvalency: a computational study. *Soft Matter* **17**, 6056 (2021).
57. A. T. Blanchard, S. Piranej, V. Pan, K. Salaita, Adhesive Dynamics Simulations of Highly Polyvalent DNA Motors. *The Journal of Physical Chemistry B* **126**, 7495 (2022/10/06, 2022).
58. C. S. Korosec, D. A. Sivak, N. R. Forde, Apparent superballistic dynamics in one-dimensional random walks with biased detachment. *Physical Review Research* **2**, 033520 (2020).
59. S. Marbach, J. A. Zheng, M. Holmes-Cerfon, The nanocaterpillar's random walk: diffusion with ligand–receptor contacts. *Soft Matter* **18**, 3130 (2022).
60. J. Lowensohn, L. Stevens, D. Goldstein, B. M. Mognetti, Sliding across a surface: Particles with fixed and mobile ligands. *The Journal of Chemical Physics* **156**, 164902 (2022).
61. S. Kovacic *et al.*, Construction and Characterization of Kilobasepair Densely Labeled Peptide-DNA. *Biomacromolecules* **15**, 4065 (2014).
62. A. L. Boyle *et al.*, Squaring the Circle in Peptide Assembly: From Fibers to Discrete Nanostructures by de Novo Design. *Journal of the American Chemical Society* **134**, 15457 (2012).
63. R. Bunk *et al.*, Guiding motor-propelled molecules with nanoscale precision through silanized bi-channel structures. *Nanotechnology* **16**, 710 (2005).
64. F. W. Lindberg *et al.*, Controlled Surface Silanization for Actin-Myosin Based Nanodevices and Biocompatibility of New Polymer Resists. *Langmuir* **34**, 8777 (2018).
65. N. Stuurman, “MTrack2 software” (UCSF, 2003).
66. Z. Chen *et al.*, Single-molecule diffusometry reveals no catalysis-induced diffusion enhancement of alkaline phosphatase as proposed by FCS experiments. *Proceedings of the National Academy of Sciences* **117**, 21328 (2020).
67. E. Kepten, A. Weron, G. Sikora, K. Burnecki, Y. Garini, Guidelines for the Fitting of Anomalous Diffusion Mean Square Displacement Graphs from Single Particle Tracking Experiments. *PLOS ONE* **10**, e0117722 (2015).
68. C. S. Korosec, Modelling and engineering artificial burnt-bridge ratchet molecular motors. PhD thesis, Simon Fraser University (2021).
69. T. N. Akopian, A. F. Kisselev, A. L. Goldberg, Processive Degradation of Proteins and Other Catalytic Properties of the Proteasome from *Thermoplasma acidophilum*\*. *Journal of Biological Chemistry* **272**, 1791 (1997).
70. M. R. Nejadnik *et al.*, Adsorption of Pluronic F-127 on Surfaces with Different Hydrophobicities Probed by Quartz Crystal Microbalance with Dissipation. *Langmuir* **25**, 6245 (2009).

71. A. Tanka-Salamon *et al.*, Structure and Function of Trypsin-Loaded Fibrinolytic Liposomes. *BioMed Research International* **2017**, 5130495 (2017).
72. M. Malmsten, K. Emoto, J. M. Van Alstine, Effect of Chain Density on Inhibition of Protein Adsorption by Poly(ethylene glycol) Based Coatings. *Journal of Colloid and Interface Science* **202**, 507 (1998).
73. Invitrogen, “Surface-activated Dynabeads” (2010).
74. Invitrogen, “Dynabeads® M-270 Amine product datasheet” (2012).
75. M. Matse, M. V. Chubynsky, J. Bechhoefer, Test of the diffusing-diffusivity mechanism using near-wall colloidal dynamics. *Physical Review E* **96**, 042604 (2017).
76. E. Schäffer, S. F. Nørrelykke, J. Howard, Surface Forces and Drag Coefficients of Microspheres near a Plane Surface Measured with Optical Tweezers. *Langmuir* **23**, 3654 (2007).

**Acknowledgments:** This project was spawned many years ago by a team grant from the Human Frontier Science Program. From this original group, we would especially like to acknowledge Laleh Samii and especially Suzana Kovacic for their work on the original Lawnmower design, Martin Zuckermann for physical insight, Dek Woolfson for stimulating ideas, and Damiano Verardo for many discussions and complementary experiments in Lund. We are grateful to our former Lund colleague Jingyuan Zhu for inspiring discussion of channel fabrication. The channels were made in Lund Nano Lab. We additionally thank present and former SFU colleagues Mike Kirkness for help with surface chemistry and critical questions, Juliette Savoye for testing of experimental protocols, David Lee for microscopy assistance, and Eldon Emberly and David Sivak for insightful theoretical discussions. Nordita is partially supported by Nordforsk.

**Funding:**

Natural Sciences and Engineering Research Council of Canada (NSERC) Discovery Grant RGPIN-2020-04680 (NRF)

NSERC Discovery Grant RGPIN-2015-05545 (NRF)

NSERC Post-Graduate Scholarship – Doctoral (CSK)

NSERC Postdoctoral Fellowship (CSK)

Swedish Research Council project 2020-04226 (HL)

Swedish Research Council project 2020-05266 (RE)

Nordforsk (RE, no specific project number)

European Union’s Horizon 2020 research and innovation programme under grant agreements No 732482 (Bio4Comp) and no 951375 (ArtMotor) (HL, PMGC)

Volkswagen Foundation Project No. 93439/93440. (HL, RL)

**Author contributions:**

Conceptualization: CSK, IU, PS, RL, HL, NRF

Formal Analysis: CSK, IU, RE, CA

Methodology: CSK, IU, PS, RL, RE, HL, NRF

Investigation: CSK, IU, PS, RL, RE

Funding acquisition: RE, HL, NRF

Supervision: HL, NRF

Project administration: NRF

Visualization: CSK

Writing – original draft: CSK, NRF

Writing – review & editing: CSK, IU, PS, RL, RE, CA, PMGC, HL, NRF

**Competing interests:** Authors declare that they have no competing interests.

### **Supplementary Materials**

Supplementary Text

Figs. S1 to S15

References (68-76)

Movies S1-S5

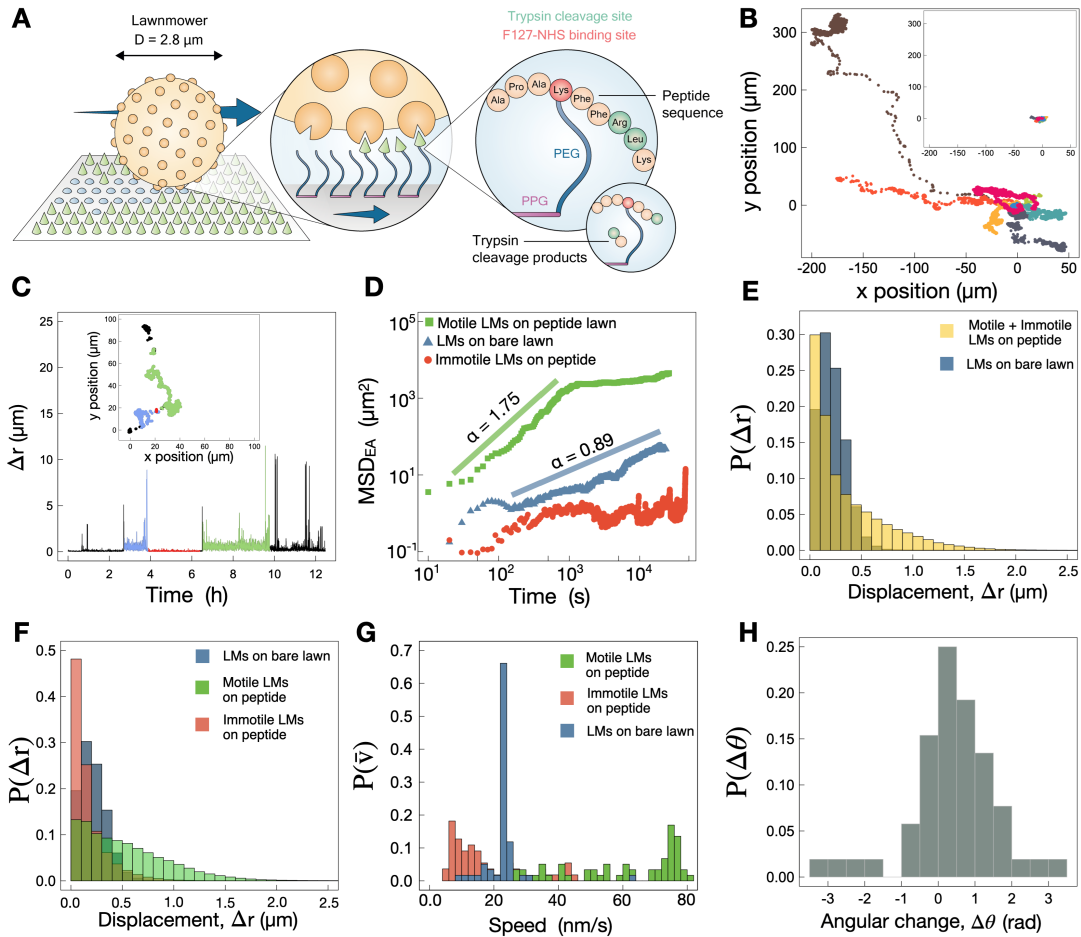


**Fig. 1. Lawnmowers exhibit motor-like dynamics on peptide lawns.** (A) 2D schematic of the LM mechanism. The Lawnmower is designed to move as a burnt-bridges ratchet (BBR) via the successive cleavage of surface-bound peptides (green cones), leaving a wake of product (blue circles). Peptide is linked to the surface via lysine to NHS-end-modified F127 (PEG-PPG-PEG). (B) Example LM trajectories on a peptide lawn spanning 6.25 hours of motion. (Trajectories of the full 12.5 hour range are shown in Fig. S2.) Trajectories are depicted as starting from a common origin. Inset: example LM trajectories on a bare lawn, also spanning 6.25 hours, travel significantly shorter distances. For an expanded view of their diffusive motion, see Fig. S3. (C) Step size  $\Delta r$  vs time throughout one 12.5-hour LM trajectory (green in panel B and Fig. S2) on a peptide lawn.  $\Delta r$  is determined for each 10-second time interval. Dynamics are saltatory, with bursts of activity interspersed with lengthy immotile dwells. The average speed of this LM is  $\bar{v} = 36$  nm/s. (D)  $\text{MSD}_{\text{EA}}(r)$  as a function of time for motile (green squares,  $n = 59$ ), and immotile (red circles,  $n = 49$ ) LMs on peptide lawn, as well as LMs on bare lawn (blue triangles,  $n = 55$ ). (E) Distributions of displacements over all 10-second intervals for all LMs on peptide and bare lawns. (F) Displacements from panel (E) are plotted separately for motile and immotile classes of LMs on peptide lawns. Small displacements of motile LMs correspond to periods of immotility within the trajectory (e.g. panel B). (G) Distributions of trajectory-averaged mean speeds of all individual motile and immotile LMs on peptide and bare lawns. LMs on bare lawns are generally much slower, with a distribution of mean speeds centred around an ensemble-average mean speed of  $\langle \bar{v} \rangle = 23 \pm 4$  nm/s.  $\langle \bar{v} \rangle$  of motile LMs on peptide lawns is significantly higher:  $\langle \bar{v} \rangle = 58 \pm 20$  nm/s. (H) Consistent with the expected BBR mechanism, long steps (here,

$\Delta r > 10 \mu\text{m}$ ) are directionally persistent, as shown by the peak in the distribution of angular changes around  $\Delta\theta = (\Delta\theta_{i+1} - \Delta\theta_i) = 0$ .

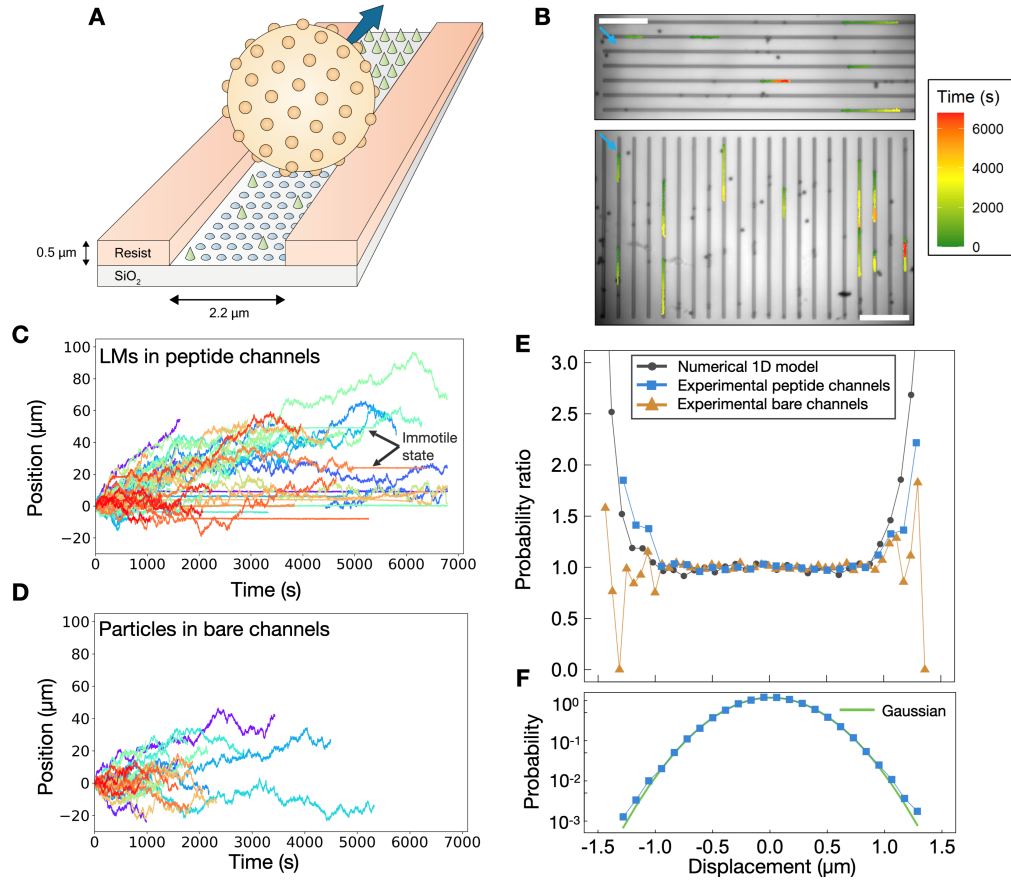


**Fig. 2. Lawnmowers exhibit track-guided motion.** (A) Schematic illustrating LM motion within a lithographically defined peptide-containing channel with polymer resist walls and a SiO<sub>2</sub> channel floor that was selectively functionalized. LM beads have a density of 1.6 g/cm<sup>3</sup> and are partially confined to the inside of channels by gravity. Channels are patterned in two directions as a control for possible background flow. (B) Trajectories of motile LM on peptide lawns, coloured from green to red to illustrate the time course of motion. Trajectories are overlaid with an image of the orthogonally patterned channels in the beginning of imaging (trajectories that started later are not depicted). The light blue arrows show the direction of slight background flow (see text). Scale bar is 50 μm. (C, D) Position along the channel direction as a function of time for (C) LMs in peptide channels and (D) particles in bare channels. The starting position of each LM is plotted with a common origin, with the positive direction chosen to align with the observed background flow in the channel. (E, F) Displacement distributions relative to Gaussian distributions. (E) Comparison of experimental and model results to Gaussian distributions. Plotted are the ratios of probability densities for the measured versus Gaussian-predicted distributions, where the first and second moments of the Gaussian distribution match experiment. Blue squares: peptide lawn from (C). Orange triangles: bare lawn from (D). Black circles: 1D LM model. The model captures the heavy tails seen for LMs on peptide lawns, while bare lawn trajectories are described by diffusion. (F) Displacement probability distribution of LMs in peptide channels has heavier tails than a Gaussian distribution, as seen also by the kurtosis of the distribution of  $\kappa = 3.3$ .

# Supplementary Materials for

The Lawnmower: an autonomous, protein-based artificial molecular motor

Chapin S. Korosec<sup>†,\*</sup>, Ivan Unksov<sup>†</sup>, Pradheebha Surendiran, Roman Lyttleton, Paul M.G. Curmi, Christopher N. Angstmann, Ralf Eichhorn, Heiner Linke<sup>\*</sup>, Nancy R. Forde<sup>\*</sup>

<sup>†</sup>Equal contributions

\*Correspondence to: [chapinskorosec@gmail.com](mailto:chapinskorosec@gmail.com), [heiner.linke@lth.lu.se](mailto:heiner.linke@lth.lu.se), [nforde@sfu.ca](mailto:nforde@sfu.ca)

## **This PDF file includes:**

Supplementary Text  
Figs. S1 to S15  
Captions for Movies S1-S5

## **Other Supplementary Material for this manuscript includes the following:**

Movies S1-S5

## Supplementary Text

### Polyvalency estimates

The original LM concept and design was introduced by Kovacic *et al.* (1), though its motility was not tested. In their work, the LM consists of a quantum dot hub decorated with trypsin enzymes (Sigma-Aldrich, T1426). Because of its small size, tracking quantum-dot motion requires fluorescence imaging. Its small size also means that it may penetrate polymer brush lawns, where it has been observed to undergo electrostatically mediated adhesion to the surface (2, 3). Furthermore, because Kovacic *et al.* determined that the multivalency of the QD LM is only  $N \approx 8$  trypsins (1), its processivity and mechanochemical performance may be quite low (4-6). A micron-sized hub with larger mass and diameter resolves this issue as the effect of gravity becomes non-negligible and the device will not diffuse away from the surface. Thus, for the work presented here we implement the Lawnmower design using a much larger, 2.8  $\mu\text{m}$ -diameter hub (Fig. S1).

The polyvalency of the microspherical LM was determined experimentally, as described in the Methods and shown in Fig. S1. Because trypsin is a nonprocessive enzyme (7), the activity of a LM scales linearly with the number of tethered, active trypsins. From this value, and literature values on the density of the polymer brush lawn, here we determine the number of trypsins and peptides found in the LM footprint.

We assume that the LM can fully indent the polymer brush, such that area of the spherical cap in contact with the lawn is  $A = 2\pi r h$  where the bead radius  $r = 1.4 \mu\text{m}$  and the height of the lawn is given by  $h$ . We estimate  $h = 12 \text{ nm}$  by adding the thickness of the F127 polymer brush ( $\sim 8.5 \text{ nm}$ , when deposited on a hydrophobic surface producing a contact angle of  $\sim 100$  degrees as was the case here (8, 9)), the length of the SMCC crosslinker used to couple the trypsin to the bead (8.3  $\text{\AA}$ ) and the diameter of the trypsin (3 nm (10)). This gives a footprint of  $A = 0.1 \mu\text{m}^2$ . With the experimentally determined trypsin density on the LM of  $0.02 \text{ nm}^{-2}$ , we find that the spherical cap can accommodate about  $2 \cdot 10^3$  trypsins. In turn, the expected peptide density is that of the PEG arms of the brush:  $0.1 \text{ nm}^{-2}$  (11), and thus the number of peptides that can contact the LM footprint is  $1 \cdot 10^4$  peptides. These values represent upper limits of trypsin and peptide number, as they have been determined assuming complete compression of the underlying polymer brush, which is unlikely to be the case.

We can compare this experimental value of polyvalency to two constraining values. First, M-270 amine Dynabeads contain an active amine density of  $\sim 150 \mu\text{mol/g}$  of beads, with a dry weight of 30 mg per  $2 \times 10^9$  beads (12, 13). This gives  $1.3 \times 10^9 \text{ NH}_2/\text{bead}$ . This number of reactive groups is easily sufficient to accommodate  $5 \times 10^5$  trypsin proteases. One can also calculate the maximum possible packing density of trypsins on the bead surface. Treating trypsins as 3 nm diameter spheres and assuming a hexagonally close-packed structure on the surface of the Dynabead (90% surface packing density), one calculates a maximum of  $3 \times 10^6$  trypsins/LM. The experimental value falls below – but reasonably close to – this maximum, suggesting these Lawnmowers are close to the maximum possible polyvalency for this hub size.

## Diffusion coefficients

The values of diffusion coefficients determined for LMs on bare 2D lawns are narrowly dispersed (Fig. S7D), with  $\langle D \rangle = 0.056 \pm 0.004 \mu\text{m}^2 \cdot \text{s}^{-1}$  ( $n = 55$ ; error is standard deviation among measurements). This value of diffusion coefficient is less than that predicted by the Stokes-Einstein equation for diffusion of a sphere free in solution,

$$D_0 = \frac{k_B T}{6\pi\eta R}, \quad (\text{S1})$$

where  $T$  is temperature,  $\eta$  the viscosity of water, and  $R$  the particle radius (here,  $1.4 \mu\text{m}$ ). Eq. S1 predicts  $D_0 = 0.18 \mu\text{m}^2/\text{s}$ . Boundary conditions (such as a planar surface in our experiments) influence the fluid flow around an object leading to an increase in drag, and therefore a decrease in diffusion coefficient (14). It is therefore expected that our diffusion coefficients are lower than predicted by Eq. S1. The diffusion coefficient for a sphere diffusing parallel to a boundary,  $D_{\parallel}$ , was developed by Faxén and is given by (15)

$$D_{\parallel} = D_0 \left( 1 - \frac{9}{16} \frac{R}{h} + \frac{1}{8} \frac{R^3}{h^3} + \frac{45}{25} \frac{R^4}{h^4} + \mathcal{O}\left(\frac{R^5}{h^5}\right) \right), \quad (\text{S2})$$

where  $h$  is the height from the surface. Using Eq. S2 for our beads with  $R = 1.4 \mu\text{m}$  that are effectively touching the surface, we calculate that  $D_{\parallel}$  is expected to be  $\sim 1/3$  of the bulk value predicted from Eq. S1. This agrees favorably with the ratio of our measured diffusion coefficient to the predicted bulk value, further supporting our conclusion that LMs are undergoing two-dimensional diffusion on bare lawns.

For LMs in channels, the variance of the parallel displacement distribution provided a similar value of the diffusion coefficient:  $D = 0.06 \mu\text{m}^2/\text{s}$ .

## Supporting References

1. S. Kovacic *et al.*, Design and Construction of the Lawnmower, An Artificial Burnt-Bridges Motor. *IEEE Transactions on NanoBioscience* **14**, 305 (2015). doi: 10.1109/TNB.2015.2393872
2. C. S. Korosec, Modelling and engineering artificial burnt-bridge ratchet molecular motors. PhD thesis, Simon Fraser University (2021).
3. I. N. Unksov *et al.*, Through the Eyes of Creators: Observing Artificial Molecular Motors. *ACS Nanoscience Au* **2**, 140 (2022).
4. L. Samii *et al.*, Time-dependent motor properties of multipedal molecular spiders. *Physical Review E* **84**, 031111 (2011).
5. C. S. Korosec, M. J. Zuckermann, N. R. Forde, Dimensionality-dependent crossover in motility of polyvalent burnt-bridges ratchets. *Physical Review E* **98**, 032114 (2018).
6. A. T. Blanchard, Burnt bridge ratchet motor force scales linearly with polyvalency: a computational study. *Soft Matter* **17**, 6056 (2021).
7. T. N. Akopian, A. F. Kisselev, A. L. Goldberg, Processive Degradation of Proteins and Other Catalytic Properties of the Proteasome from *Thermoplasma acidophilum*\*. *Journal of Biological Chemistry* **272**, 1791 (1997).
8. M. R. Nejadnik *et al.*, Adsorption of Pluronic F-127 on Surfaces with Different Hydrophobicities Probed by Quartz Crystal Microbalance with Dissipation. *Langmuir* **25**, 6245 (2009).
9. M. W. H. Kirkness, C. S. Korosec, N. R. Forde, Modified Pluronic F127 Surface for Bioconjugation and Blocking Nonspecific Adsorption of Microspheres and Biomacromolecules. *Langmuir* **34**, 13550 (2018).
10. A. Tanka-Salamon *et al.*, Structure and Function of Trypsin-Loaded Fibrinolytic Liposomes. *BioMed Research International* **2017**, 5130495 (2017).
11. M. Malmsten, K. Emoto, J. M. Van Alstine, Effect of Chain Density on Inhibition of Protein Adsorption by Poly(ethylene glycol) Based Coatings. *Journal of Colloid and Interface Science* **202**, 507 (1998).
12. Invitrogen, “Surface-activated Dynabeads” (2010).
13. Invitrogen, “Dynabeads® M-270 Amine product datasheet” (2012).
14. M. Matse, M. V. Chubynsky, J. Bechhoefer, Test of the diffusing-diffusivity mechanism using near-wall colloidal dynamics. *Physical Review E* **96**, 042604 (2017).
15. E. Schäffer, S. F. Nørrelykke, J. Howard, Surface Forces and Drag Coefficients of Microspheres near a Plane Surface Measured with Optical Tweezers. *Langmuir* **23**, 3654 (2007).

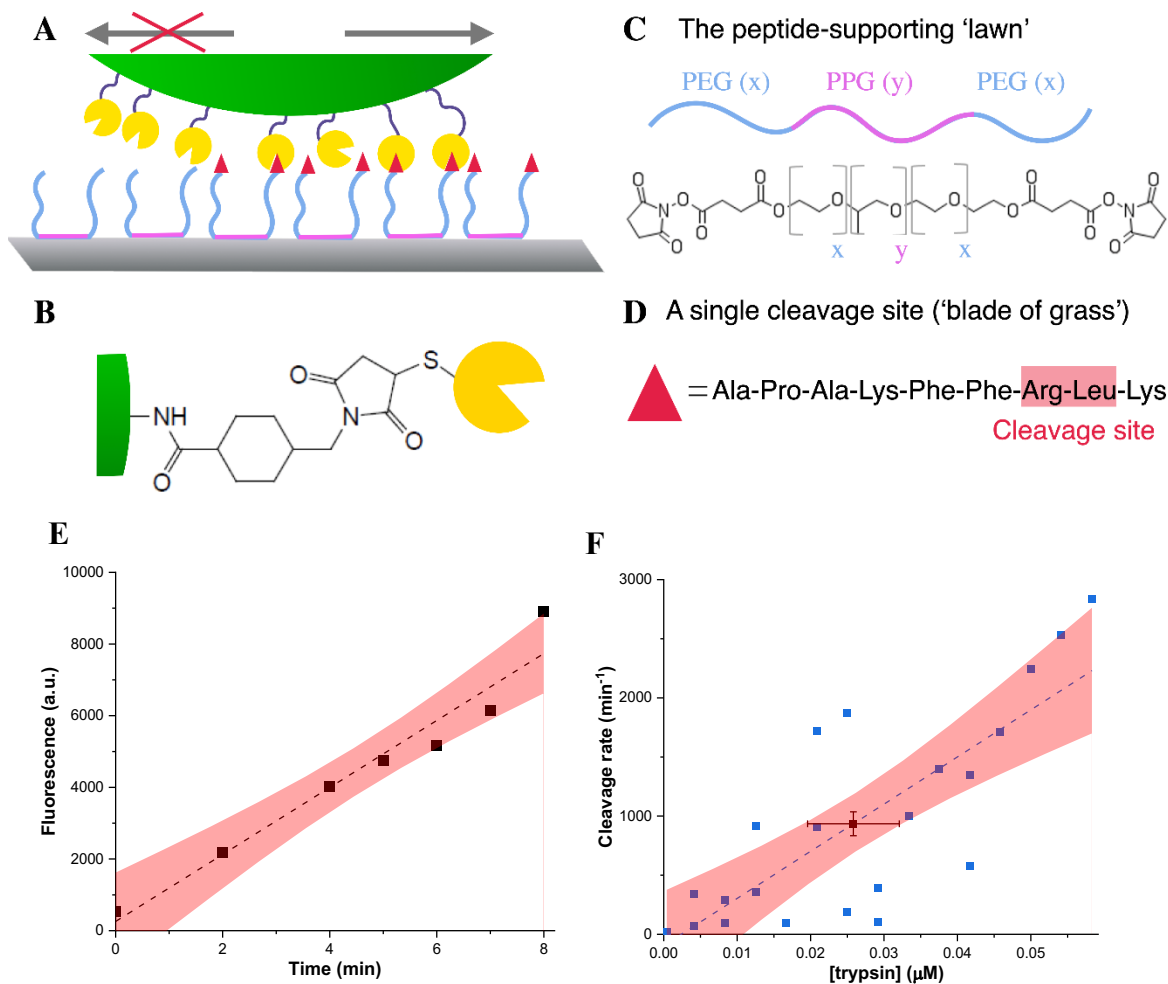


**Fig. S1. Details of Lawnmower design and construction**

(A) The Lawnmower molecular motor concept is based on a burnt-bridge ratchet design. In the current design the LM consists of a central Dynabead hub (diameter: 2.8 μm) to which trypsin proteases are bound. (B) Each protease is linked to the hub via a heterobifunctional polymer linker (sulfo-SMCC). (C) The triblock copolymer lawn chemistry is used from ref. (9). Shown is a single NHS-F127 polymer, with NHS moieties on each of the terminal PEG groups. (D) A 'blade of grass' from the lawn is the peptide substrate, with the site of trypsin cleavage shown. The peptide is linked to the NHS-F127 via its central lysine sidechain. (E) Fluorescence arising from cleavage of fluorogenic peptides by LMs at a concentration of  $3 \cdot 10^7$  LMs/mL. (F) Cleavage rates for different concentrations of trypsin (blue dots) and the same concentration of peptides as in (E). The cleavage rate of LMs (dark red dot) matches with the cleavage rate of trypsin at  $(2.6 \pm 0.6) \cdot 10^{-8}$  M within a 95% confidence band (pink). Significant dispersion of the reference measurements may be attributed to autocleavage of trypsin in bulk solution.

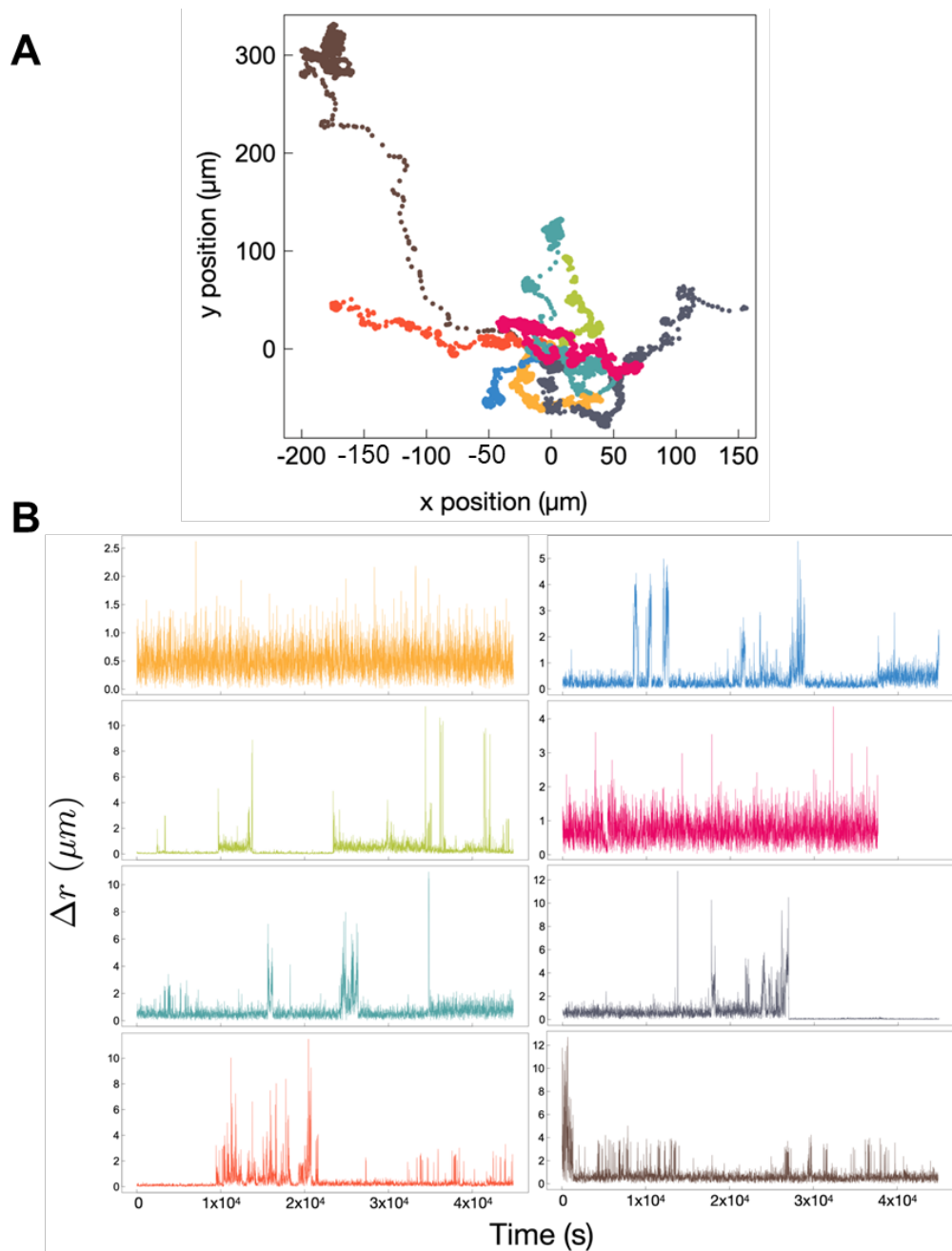


**Fig. S2.**

(A) Representative LM trajectories on a peptide lawn from Fig. 1B, here shown over the entire 12.5-hour measurement time. (B) LM displacements vs time indicate highly heterogeneous dynamics. Displacements  $\Delta r$  are determined per 10-second time interval, for the exemplary LM trajectories shown in panel (A) and Fig. 1B, color-coded accordingly. Note: the vertical scale varies among panels.

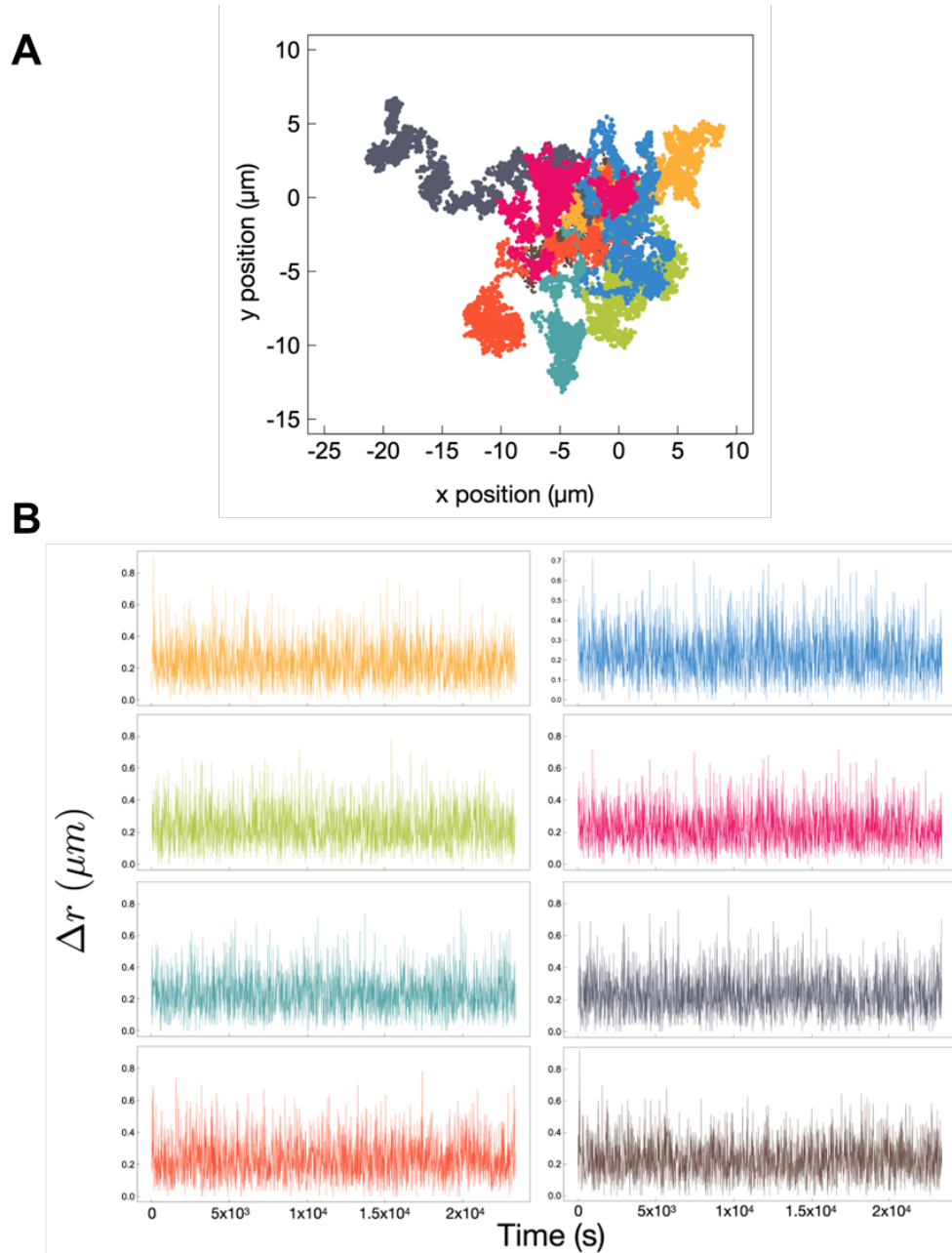


**Fig. S3.**

(A) Representative LM trajectories on a bare lawn from Fig. 1B inset, here shown at a larger scale to more clearly show their diffusive nature. (B) LM displacements vs time indicate homogeneous dynamics, in stark contrast to dynamics on a peptide lawn (Fig. S2). Displacements  $\Delta r$  are determined per 10-second time interval, for the exemplary LM trajectories shown in panel (A) and in the inset to Fig. 1B, color-coded accordingly. Note: the vertical scale varies slightly among panels.

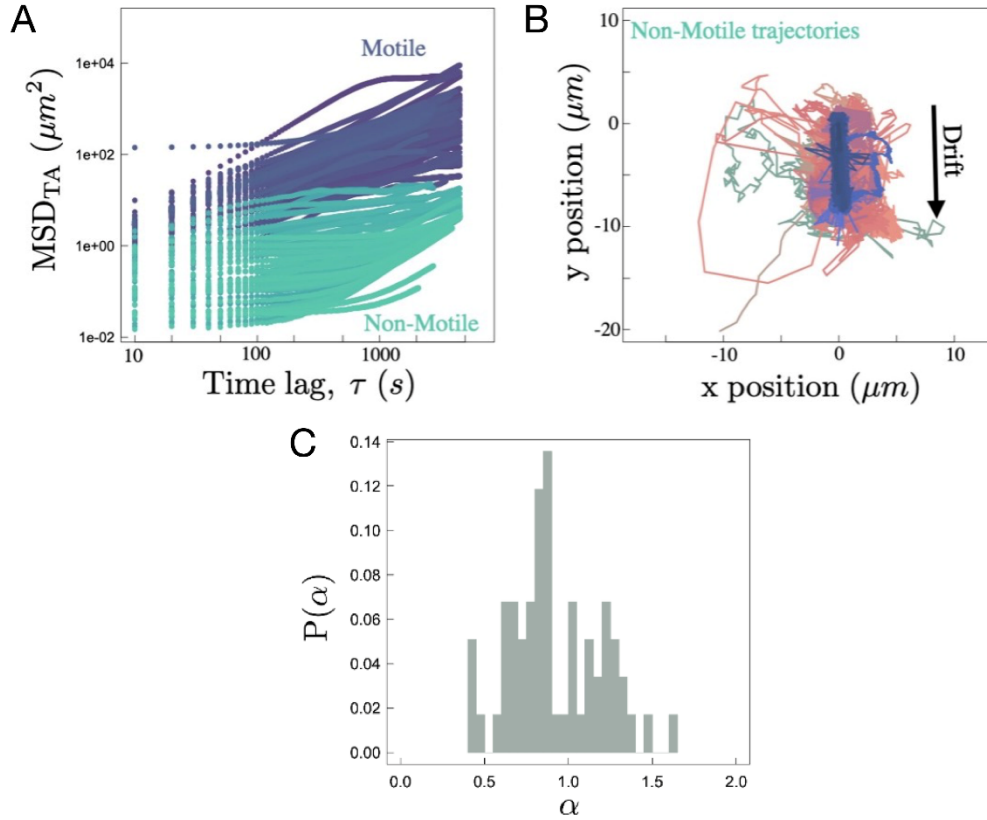


**Fig. S4.**

(A)  $\text{MSD}_{\text{TA}}$  of each LM on a peptide lawn in a single experiment. Trajectories are classified as motile or non-motile based on a threshold of  $\text{MSD}_{\text{TA}} = 10 \mu\text{m}^2$  at  $\tau = 4400 \text{ s}$  (the longest time lag plotted and used for all MSD analysis of LMs on peptide lawns). (B) A plot of all non-motile trajectories in one 12.5 hr experiment ( $n = 49$ ), centered at a common origin. Because of their extensive overlap, we concluded that the majority were irreversibly bound to the surface and thus used the average of these displacements as a stage drift trajectory. The drift trajectory was then subtracted from each motile LM's trajectory to correct for sample drift, prior to further analysis. Each non-motile trajectory is plotted with a unique color to help visually distinguish between trajectories. (C) Histogram of  $\alpha_{\text{TA}}$  for each motile LM trajectory on a peptide lawn ( $n = 59$ ). For each trajectory,  $\alpha_{\text{TA}}$  was determined from a linear fit of its  $\log(\text{MSD}_{\text{TA}})$  vs  $\log(\tau)$  over all time lags from  $\tau_{\text{min}} = 10 \text{ s}$  to  $\tau_{\text{max}} = 0.1 T_{\text{msr}}$ , representing 10% of the total measurement time of  $T_{\text{msr}} = 12.5 \text{ hours}$  for the peptide lawn. Individual motile LMs on peptide lawns display a range of anomalous diffusive dynamics ranging from subdiffusive ( $\alpha = 0.5$ ) to superdiffusive ( $\alpha = 1.4$ ).

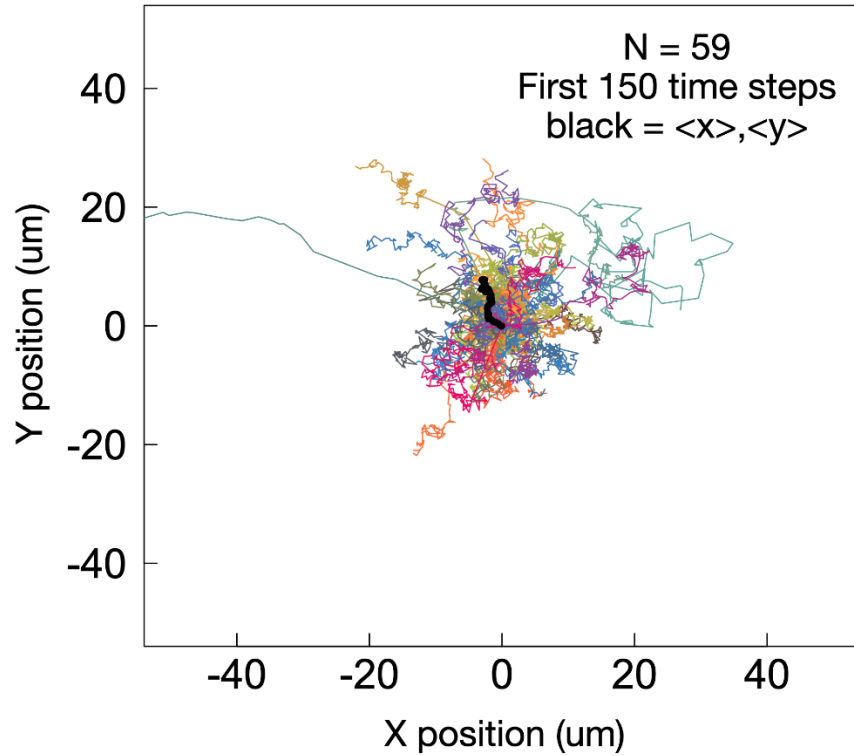


**Fig. S5.**

All  $n=59$  motile Lawnmower trajectories over the first 1500 seconds when  $\alpha_{EA}$  is strongly superdiffusive, displayed from a common origin. The superdiffusive dynamics do not arise from sample drift, as the trajectories visually appear isotropically distributed; the thick black line indicates the mean trajectory.

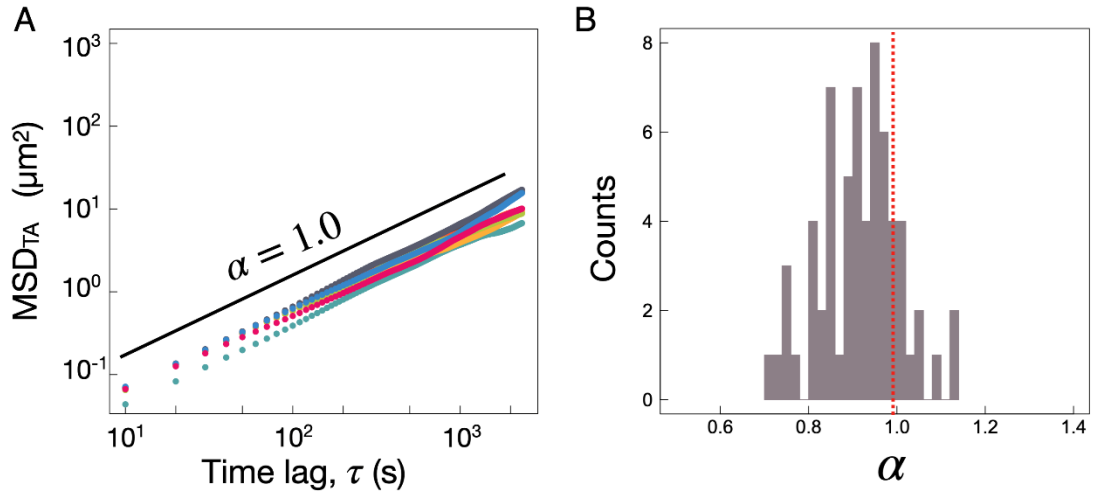


**Fig. S6.**

(A) The  $\text{MSD}_{\text{TA}}$  of all LMs on bare lawns throughout a single experiment of 6.25 hours. (B) Histogram of  $\alpha_{\text{TA}}$  for each LM trajectory on a bare lawn ( $n = 55$ ). For each trajectory,  $\alpha_{\text{TA}}$  was determined from a linear fit of its  $\log(\text{MSD}_{\text{TA}})$  vs  $\log(\tau)$  over all time lags from  $\tau_{\min} = 10$  s to  $\tau_{\max} = 0.1T_{\text{msr}}$ , representing 10% of the total measurement time of  $T_{\text{msr}} = 6.2$  hours on the bare lawn. LMs on bare lawns exhibit  $\alpha$  values clustered more closely around  $\alpha = 1$ , exemplifying more conventionally diffusive dynamics.

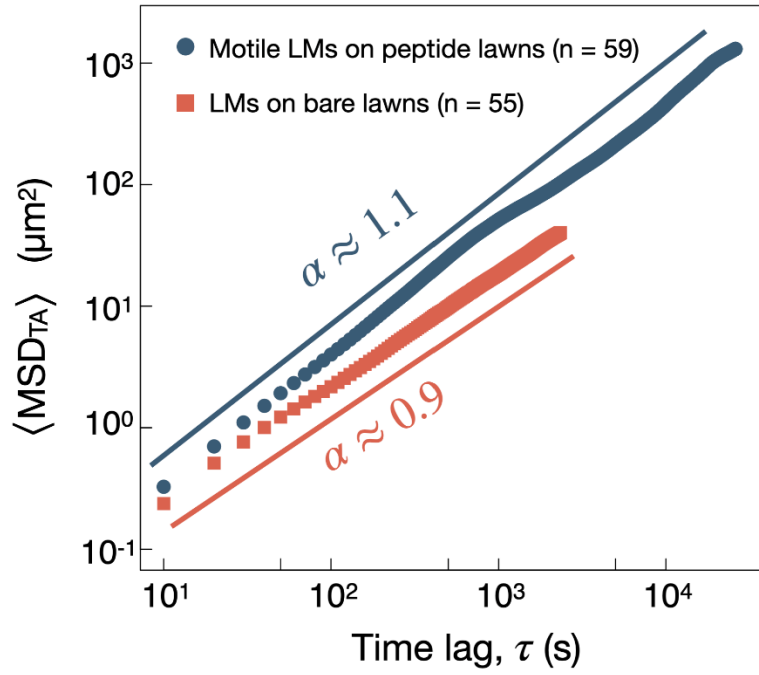


**Fig. S7.**

The ensemble-averaged MSD<sub>TA</sub>,  $\langle \text{MSD}_{\text{TA}} \rangle$ , on peptide lawns and on bare lawns. Slightly superdiffusive dynamics are apparent throughout the 12.5-hour long trajectories of motile LMs on peptide lawns, while on bare lawns, LM motility is slightly subdiffusive.

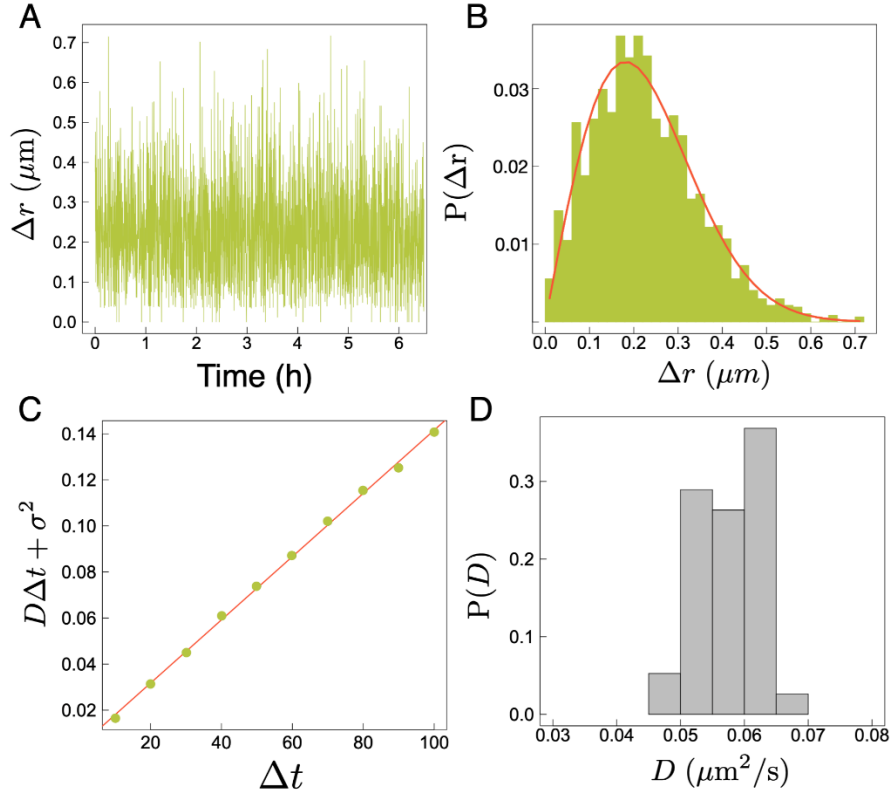


**Fig. S8.**

Lawnmower displacement distributions on a bare lawn are well described by conventional diffusion in 2D. (A) Representative plot of the time-dependent LM displacement  $\Delta r$  in each 10-second time interval throughout one trajectory (colored green in the inset to Fig. 1B and in Fig. S3). (B) Probability distribution of displacements. Red line is a fit with the Rayleigh distribution describing conventional 2D diffusion (Eq. 1). (C) Fits to the displacement distributions at different  $\Delta t$  give estimates of  $D\Delta t + \sigma_t^2$  where  $D$  is diffusion coefficient and  $\sigma_t^2$  is tracking noise. For this trajectory, a linear fit provides  $D = 0.051 \mu\text{m}^2/\text{s}$  and  $\sigma_t^2 = 0.0051 \mu\text{m}^2$ . (D) Distribution of diffusion coefficients for all LMs on bare lawns, where  $D$  is determined for each trajectory as in panel (C). The results are tightly clustered, indicating homogeneous LM dynamics on bare F127 lawns. The average values across the ensemble are  $\langle D \rangle = 0.056 \pm 0.004 \mu\text{m}^2/\text{s}$  and  $\langle \sigma_t^2 \rangle = 0.0024 \pm 0.0017 \mu\text{m}^2$  ( $n = 55$ ; error represents standard deviation).

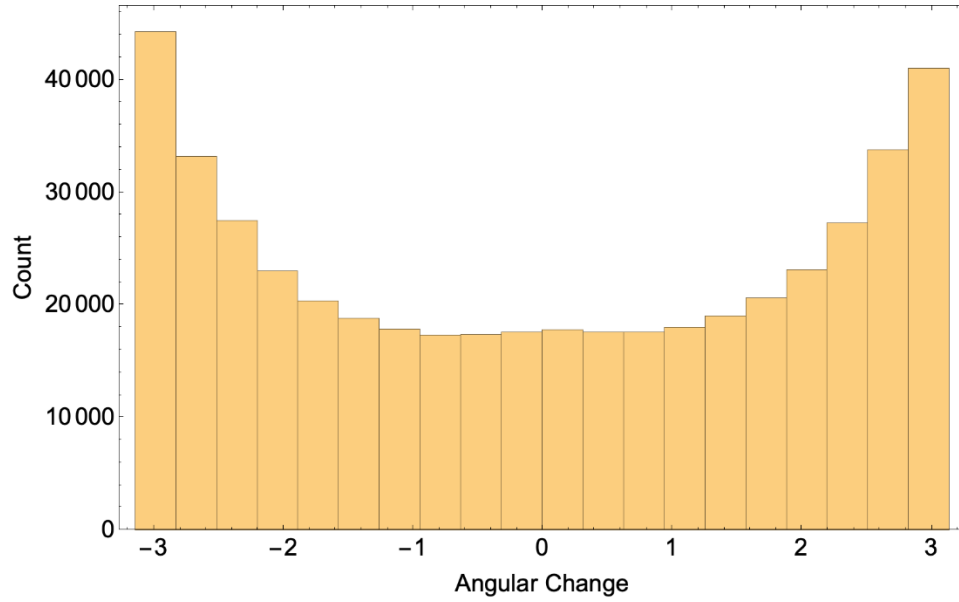


**Fig. S9.**

Distribution of angular change in direction between consecutive steps separated by  $\Delta t = 10$  s for all LMs on peptide lawns,  $\Delta\theta = (\Delta\theta_{i+1} - \Delta\theta_i)$ , measured in radians. The peaks at  $\pm\pi$  indicate that it is more likely for a LM to reverse its motion in consecutive intervals. This would be expected for an elastic restoring force associated with LM-peptide binding interactions.

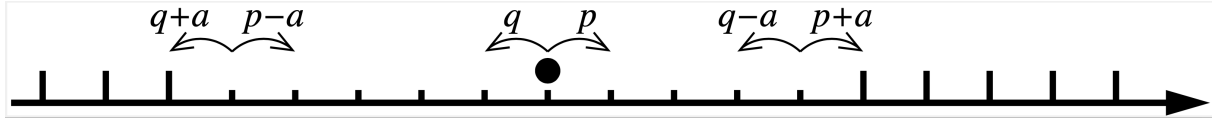


**Fig. S10.**

Simple model for the LM in 1D. The short vertical lines represent positions the LM has visited already, corresponding to an area of bare lawn. The long vertical lines represent unvisited positions with uncleaved lawn. In the region of bare lawn the LM is a usual random walker with probabilities  $q, p$  to jump to the left/right, respectively, with  $p + q = 1$ . For an unbiased random walker,  $p = q = 1/2$ ; an overall net drift can be accounted for by setting  $q = 1/2 - \delta, p = 1/2 + \delta$  ( $-1/2 \leq \delta \leq 1/2$ ). At the edges of the bare region, stepping towards an uncleaved position is favored by the enzymatic action  $a$  ( $0 \leq a \leq 1/2$ ), by adjusting  $q$  and  $p$  as indicated in the figure. If the LM moves to an uncleaved position, this position is cleaved and becomes part of the bare region.

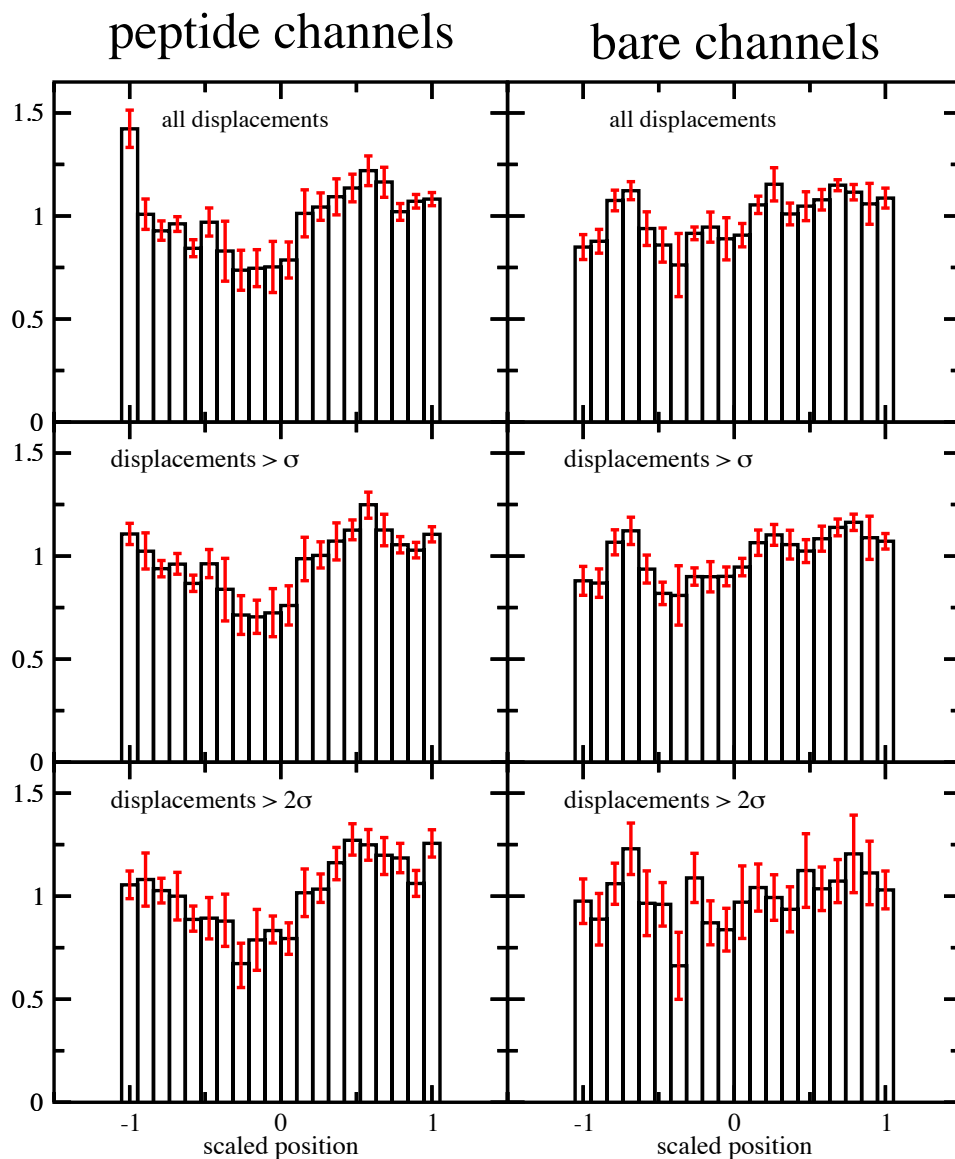


**Fig. S11.**

Histogram ratios for the scaled positions of experimentally measured displacements vs. diffusive displacements. Left column: LM data. Right column: data from the control experiment with bare lawn. First row: all displacements are shown. Second row: only displacements larger than  $\sigma$  have been counted. Third row: only displacements larger than  $2\sigma$  have been counted. The small left-right asymmetry visible in the data is probably due to an imperfect compensation of the background flow in the trajectory data (the net drift estimated from the average displacement per frame does not match the real background flow). The difference between the peptide and bare

lawn channels is the pronounced dip in the histograms around the center (i.e. around scaled position 0), which is visible in all panels for the peptide channels but not the bare channels. More precisely, the bare channel histograms are consistent, within their statistical errors, with the hypothesis of a uniform histogram in each panel, because the difference in height between individual histogram bars is comparable to the size of the error bars. In contrast, for the peptide channels the difference in height between the histogram bars in the middle region and at the edges is several error bar sizes (and, moreover, is more systematic than for the bare channels), making it extremely unlikely that the peptide channel data is statistically consistent with a uniform histogram.

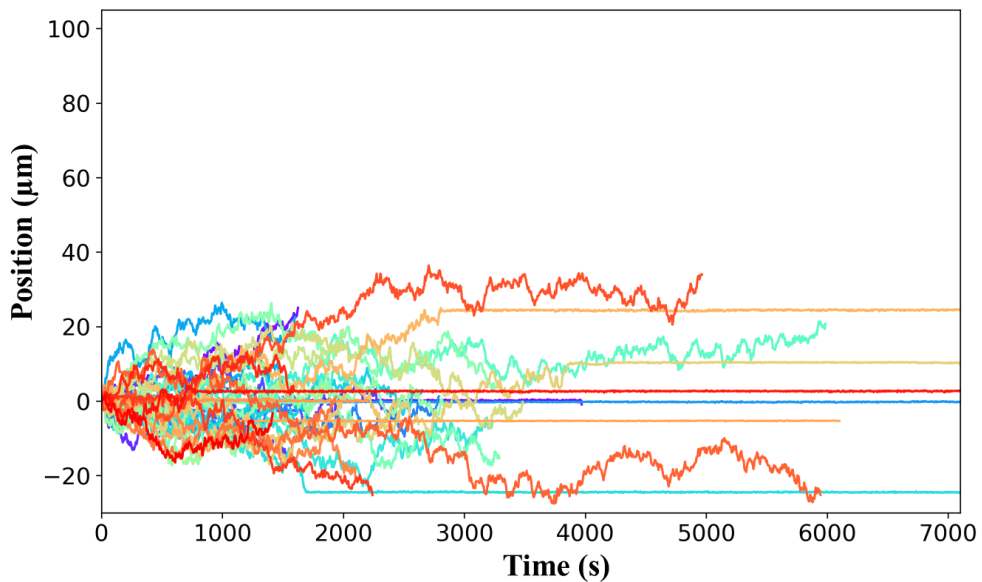


**Fig. S12.**

Trajectories from an independent replicate of LMs in peptide channels, in which some LMs show long periods of immotility. For this experiment, the kurtosis of the displacement distribution – excluding immotile portions of the trajectories – is  $\kappa = 2.97$  at a time lag of  $\tau = 5$  s (the sampling time) and  $\kappa = 3.03$  at  $\tau = 10$  s.

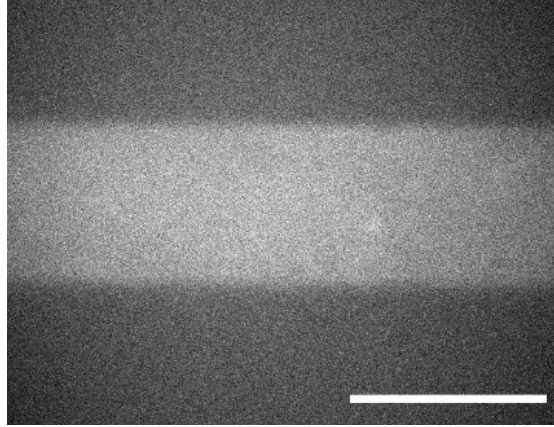


**Fig. S13.**

Selective deposition of the lawn is revealed by fluorescence imaging: cleaved peptide lawn is seen only in the channel, supported on a SiO<sub>2</sub> substrate. This experiment shows a wider channel than used for guiding LM motion. Scale bar 100 μm.

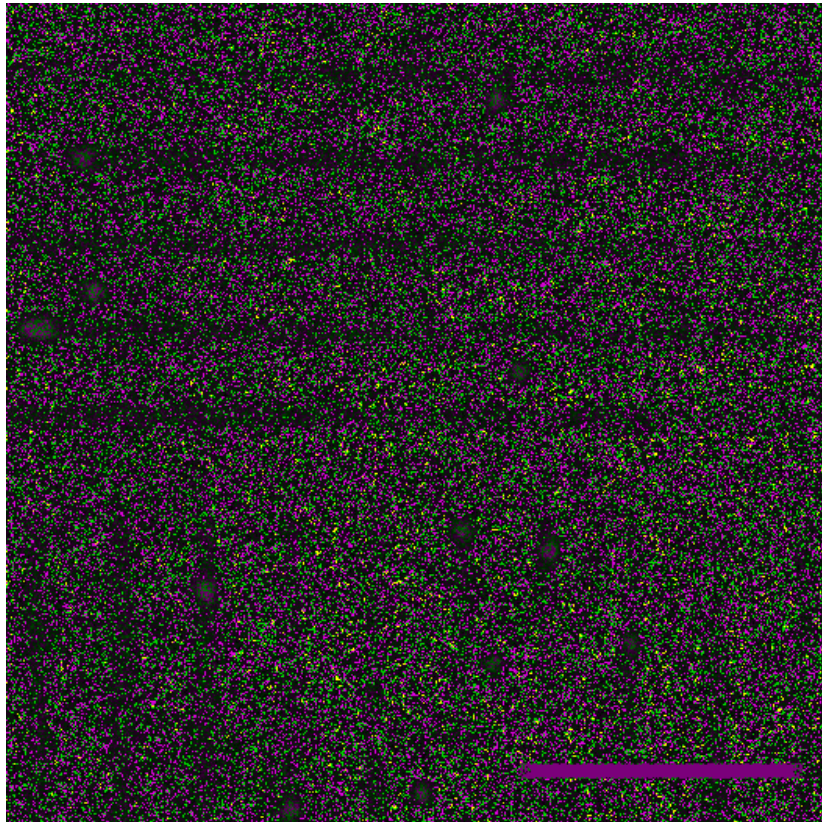


**Fig. S14.**

Fluorescence from cleaved peptides is selectively associated with channels of width 2.2  $\mu\text{m}$  used in these LM experiments. Channel fluorescence was too faint to be detected after 1.5 hours of LM motion and also after addition of 50  $\mu\text{g}/\text{ml}$  trypsin. Fluorescence was detectable after addition of 500  $\mu\text{g}/\text{ml}$  trypsin, as shown here. Autofluorescence of the Dynabeads used in LM construction enables their visualization by fluorescence microscopy, seen as large dots in this image. Scale bar: 50  $\mu\text{m}$ .

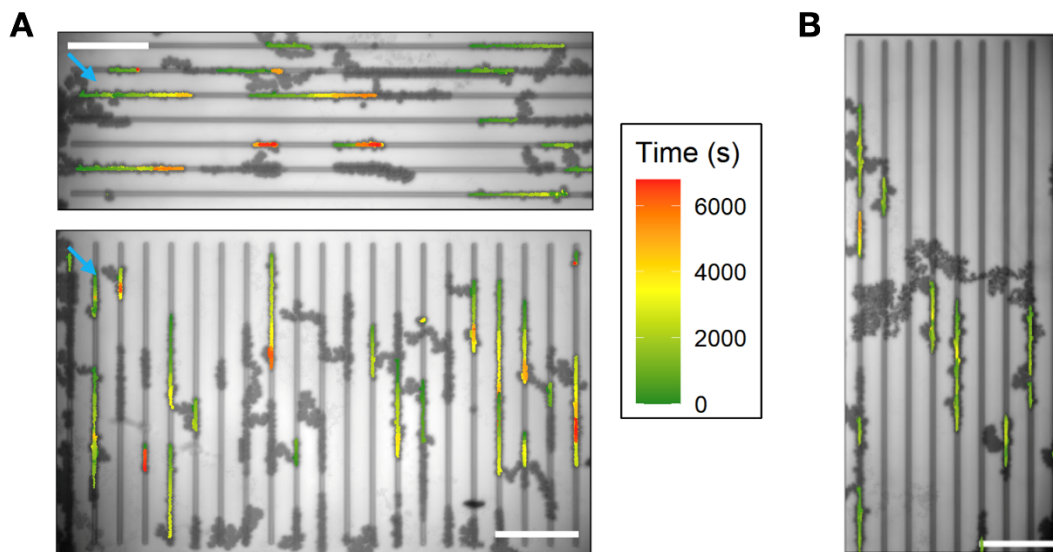


**Fig. S15.**

LMs and bare beads undergo occasional excursions out of their channels. (A) Overlay of all images in a LM channel experiment, where dark outlines show paths of LMs (sometimes escaping from one channel and diffusing into another). Trajectories included in Fig. 2 of the manuscript and our analysis are color-coded by their duration. These remain confined within a single track throughout the trajectory, and do not collide with other particles or ends of the channels. Blue arrows indicate the direction of the background drift (horizontal  $0.011 \pm 0.002$  mm/s, vertical  $0.007 \pm 0.001$   $\mu$ m/s). Scale bar is 50  $\mu$ m. (B) Similar overlay and analyzed trajectories of unmodified beads on bare lawn channels. Here all the channels had the same orientation. Scale bar is 50  $\mu$ m.

**Movie S1.**

Movie showing two Lawnmowers (2.8  $\mu\text{m}$  diameter; black circles) on a 2D peptide lawn, one motile and the other immotile. Movie plays at 100X real time.

**Movie S2.**

Lawnmowers in peptide channels of two orthogonal orientations. Frame rate of the videos is 50 frames/s, actual imaging frame rate is 1 frame/s. Scale bar is 50  $\mu\text{m}$ . Close-ups of selected trajectories enframed in yellow are in Movies **S3** and **S4**.

**Movies S3, S4.**

Two selected Lawnmowers (corresponding regions in Movie **S2** are marked in yellow) demonstrate prolonged immotile periods after which the motion continues. The LMs eventually jumped away from the channels, and further frames were cut off in the videos. Frame rate is 50 frames/s, scale bar is 15  $\mu\text{m}$ .

**Movie S5.**

Particles in bare channels of one orientation. Frame rate of the videos is 50 frames/s. The actual imaging frame rate was 1 frame/s. Scale bar is 50  $\mu\text{m}$ .